SENSORS & TRANSDUCERS

ISSN 1726-5479

vol. 258

4/22

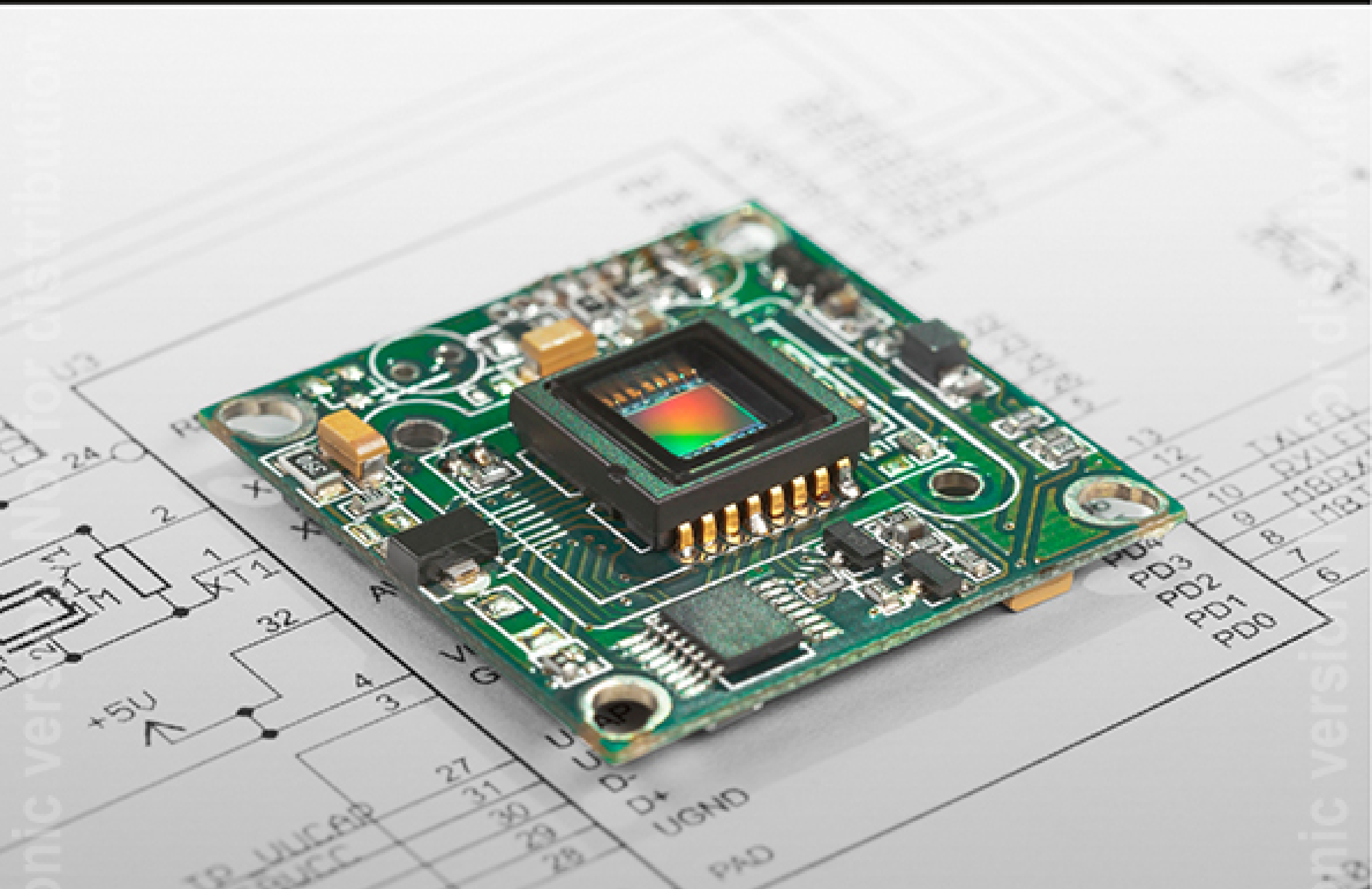

Optical Sensors & Devices: Design and Applications

International Frequency Sensor Association Publishing

IFSA

Sensors & Transducers

International Official Open Access Journal of the International Frequency Sensor Association (IFSA) Devoted to Research and Development of Sensors and Transducers

Volume 258, Issue 4, July 2022

IFSA Publishing: Barcelona • Toronto

Published by International Frequency Sensor Association (IFSA) Publishing. Printed in the USA.

Sensors & Transducers

Volume 258, Issue 4
July 2022

www.sensorsportal.com

e-ISSN 1726-5479
ISSN 2306-8515

Sensors & Transducers journal is an open access, peer review international journal published monthly by International Frequency Sensor Association (IFSA).
Available in both: print and electronic (printable pdf) formats.

Sensors & Transducers Journal

Contents

Volume 258
Issue 4
July 2022

www.sensorsportal.com

ISSN 2306-8515
e-ISSN 1726-5479

Research Articles

Optomechanical Mode-Shape Mapping in the Presence of Crosstalk
Timo Sommer, David Hoch, Kevin-Jeremy Haas, Leopold Moller, Julius Röwe, Aditya Yadav, Pedro Soubelet, Jonathan J. Finleyand Menno Poot 1

Terahertz Optoelectronic Devices Based on Three-Dimensional Modelling of Symmetrically Coupled Surface Plasmon Polariton Resonances in Bulk Dirac Semimetal
Tony Mathew Blessan, M. Gayathri, T. Alagesan, N. Yogesh 10

High-speed Wavelength Division Multiplexing Transmission over SI-Polymer Fibers
Ulrich H. P. Fischer and Mladen Jóncic 18

Preflight Preparations for Active Debris Removaland Ranging
Claude Phipps and Christophe Bonnal 25

Propagation of Azimuthally Polarized Bessel-Gaussian Beam through Helical Axicon
Ibrahim G. H. Loqman, Abdu A. Alkelly and Hassan T. Alahsab 31

Study of Polycarbonate Wettability and its Antibacterial Properties after Excimer Laser Irradiation at the Ablation Threshold Fluence
Sahar Sohrabi, Hedieh Pazokian, Bijan Ghafary, Mahmood Mollabashi and Mohsen Montazeralghaem 36

Authors are encouraged to submit article in MS Word (doc) and Acrobat (pdf) formats by e-mail: editor@sensorsportal.com. Please visit journal's webpage with preparation instructions: http://www.sensorsportal.com/HTML/DIGEST/Submition.htm

International Frequency Sensor Association (IFSA).

Sensors & Transducers, Vol. 258, Issue 4, July 2022, pp. 1-9

Sensors & Transducers

Published by IFSA Publishing, S. L., 2022
http://www.sensorsportal.com

Optomechanical Mode-Shape Mapping in the Presence of Crosstalk

[1,2] Timo SOMMER, [1,2,3] David HOCH, [1] Kevin-Jeremy HAAS, [1] Leopold MOLLER, [1] Julius RÖWE, [1] Aditya YADAV, [1,4] Pedro SOUBELET, [1,2,4] Jonathan J. FINLEY and [1,2,3,*] Menno POOT

[1] Department of Physics, Technical University of Munich, 85748 Garching, Germany
[2] Munich Center for Quantum Science and Technology (MCQST), 80799 Munich, Germany
[3] Institute for Advanced Study, Technical University of Munich, 85748 Garching, Germany
[4] Walter Schottky Institute, Technical University of Munich, 85748 Garching, Germany
[1] Tel.: +49 89 289 12358, fax: +49 89 289 12536
E-mail: menno.poot@tum.de

Received: 2 June 2022 /Accepted: 5 July 2022 /Published: 29 July 2022

Abstract: Visualizing eigenmodes is crucial for understanding the dynamics of state-of-the-art micromechanical devices. A method is established to map modes of mechanical structures optically. This fast and robust method, based on parallel modified phase-lock loops outperformed three alternative approaches. The setup used is discussed here in more detail, and the modal decomposition results are investigated further, including a study of the orthogonality of the eigenmodes and the mixing of degenerate modes. Crosstalk, however, remained a problem, especially for membranes with a small mechanical response. The issue is investigated using numerical simulations of the phase-lock loop operation, which indicate that without crosstalk compensation, the mode maps will be strongly distorted. To solve this, the phase-lock loop is equipped with crosstalk compensation and it is shown that now also in the presence of strong crosstalk, where resonances and phase responses are distorted, accurate maps are obtained.

Keywords: Optomechanics, Mode-mapping, MEMS, Phase-lock loop, Silicon-nitride, Membrane, Crosstalk.

1. Introduction

With the rapid developments in opto- and electromechanical systems [1], efficient methods for mode mapping are instrumental [2, 3]. A number of techniques to visualize mechanical modes have been developed, including optical interferometry [4, 5, 6], heterodyne detection [7, 8], dark field imaging [9, 4], and force microscopy [10-13]. However, most of these have one or more drawbacks, such as poor sensitivity, lack of phase information, low spatial resolution, or long measurement times. We experimentally demonstrated a method that combines the high sensitivity of the optical interferometric techniques with demodulation and frequency tracking to offer rapid and robust imaging of multiple modes simultaneously [2]. This enables quantitative analysis of the eigenmodes, which is further elaborated in Sec. 2.1. Crosstalk, however, turns out to be detrimental in this method, leading to unstable operation of the phase-lock loop (PLL) and distorted mode maps. Here, we demonstrate how this can be compensated, and it is shown that the newly developed mode visualization technique now even works in the presence of severe crosstalk.

2. Efficient Mode Mapping

The method can be used with a wide variety of resonators and readout and excitation schemes; its use is illustrated with interferometric measurements of the local displacement of a square Si_3N_4 membrane that is driven using a piezo. Photographs of the setup used to perform the measurement are shown in Fig. 1; for a schematic representation, see Ref. [2]. In short, by focusing light of a HeNe laser with a 10× objective onto the membrane, measuring the reflected light enables sensitive displacement detection with a lateral resolution of a few micrometers. The lowest flexural modes are at a few MHz, and their quality factors are ~ 10^5. From the observed frequencies, certain modes can be identified unambiguously, but for degenerate modes that is not possible, and their mode profile has to be visualized.

The easiest method is to drive the mode resonantly at f_0 and to record the response while scanning over the membrane. However, especially for high-quality resonators, drift of the frequency will result in inaccurate mode maps [2]. A way to circumvent this is to use a phase-lock loop (PLL) that adjusts the driving frequency in order to keep the measured phase $\phi=\angle Z$ at the set point $\phi_{setpoint}$, tracking f_0. However, this causes problems e.g. when crossing nodal lines. This is solved by taking a modulo π of the error signal e_j and by only updating the frequency when the signal $|Z|$ exceeds a threshold Z_{min}:

$$\begin{aligned} e_j &= \phi - \phi_{\mathrm{setpoint}} \mod \pi \\ f_{n+1} &= f_1 + P e_n + I \sum_{j=1}^{n} e_j \text{ for } |Z| > Z_{\min} \end{aligned} \quad (1)$$

where P is the proportional coefficient, and I is the integral coefficient of this PI-controller. With this improved PLL method, the modes can be mapped accurately and efficiently. Fig. 2 shows measured mode maps of the first 6 modes of the membrane, as well as a triplet near 7.3 MHz (bottom) which looks very complex, but are in fact superpositions of the degenerate (1,7), (7,1) and (5,5) modes.

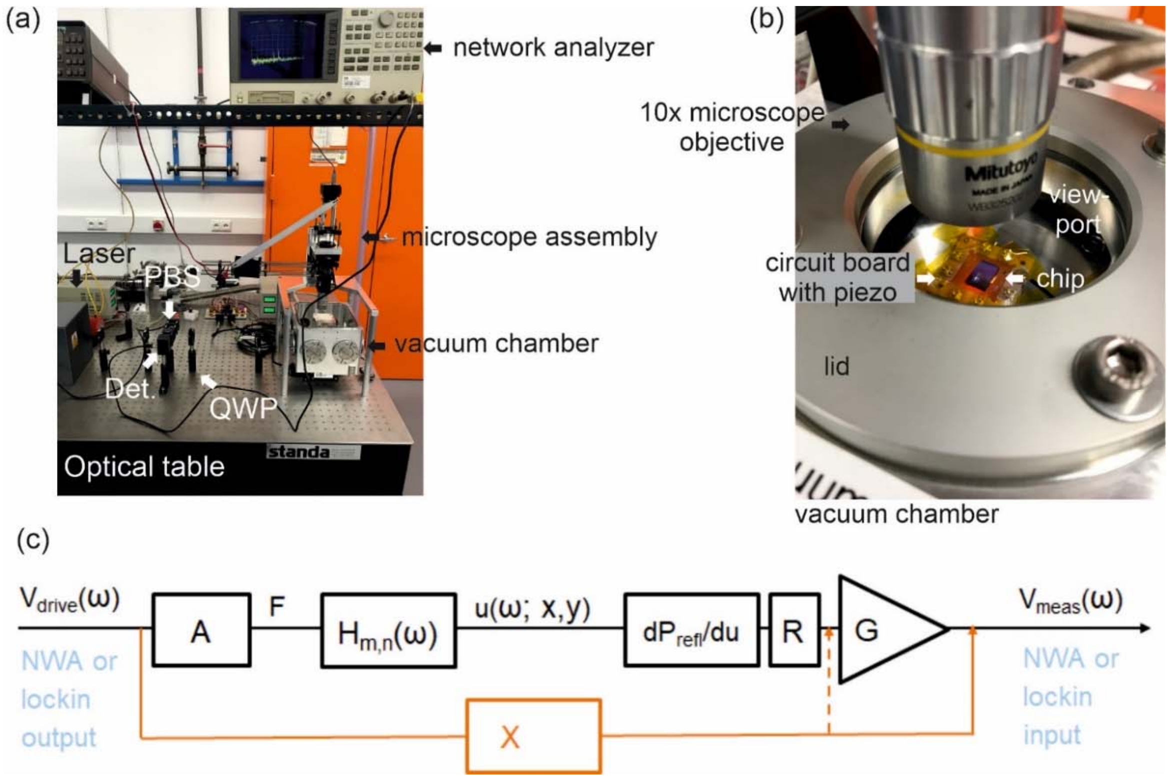

Fig. 1. (a) Photograph of the measurement setup (for clarity an early version of the setup is shown). Inside the gray box there is a HeNe laser (Melles Griot 05-LHP-151), a neutral density filter, as well as a shutter to block the beam. The driven measurements can be done using either the network analyzer shown (HP 4396A) or a lockin amplifier (Zurich Instruments HF2, not shown). Det.: photo detector (Newport 818-BB-21). PBS: polarizing beam splitter, QWP: quarter wave plate (b) Detailed view of the inside of the vacuum chamber with a mounted sample. The chip is glued onto a piezo element, which is in turn installed on a printed circuit board. (c) Linear-system equivalent of the setup. The driving voltage V_{drive} is converted into a motion of the piezo electric element (A) that results in an inertial force F on the membrane. The different eigenmodes, labeled with m,n, convert this force into a displacement (u) using the response function of the harmonic oscillator (H). Using the objective, the resulting displacement u is measured at location (x,y) via the change in reflected laser light (dP_{ref}/du). This is converted to a voltage by the photo detector with responsivity R. The signal is amplified using a low-noise amplifier with gain G. In addition to this direct pathway, there is also a crosstalk component present in the measured signal V_{meas}, as represented by $X(\omega)$.

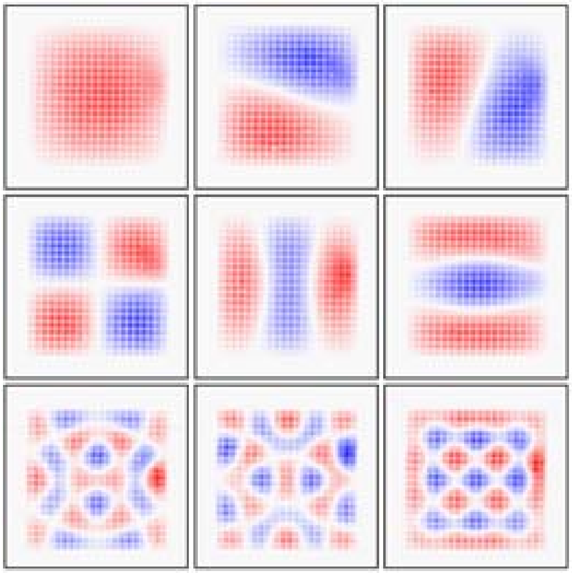

Fig. 2. Top row: measured mode maps for the (1,1), (1,2) and (2,1) mode of a 375×375µm square SiN membrane. Middle: (2,2), (3,1) and (1,3) modes. Bottom: superpositions of the (1,7), (7,1) and (5,5) triplet modes.

2.1. Mode Decomposition

The accuracy of the method even allows quantitative determination of the coefficients of the different basis functions in the measured mode maps [2]. In practice, this is done by taking the data of the individual maps, and performing linear fitting using the left matrix divide functionality of Matlab:

```
w = shapes \ map                    (2)
```

Here, w is the variable that contains the weights, map is the column vector containing the measured mode map, and shapes contain the theoretical mode maps as columns. For an $m \times n$ map and N modes for the decomposition, map is of size $m{\cdot}n \times 1$ and shapes is $m{\cdot}n \times N$. The code in Eq. (2) immediately solves the least-squares linear fitting problem for the N elements of w. Since the actual magnitude of the weights is often not that relevant, the obtained values are divided by norm(w). Using the theory of this framework, it is also possible to obtain an estimate for the uncertainty in the fitted weights [14]. However, we find it easier to use Matlab's fit function for this; the uncertainty for the decomposition is only 0.004 for all weights and this allows for a number of tests. First of all, Fig. 3(a) shows a bar plot of the weights of the different (m,n) modes, i.e. "basis functions" $\xi_{m,n}(x,y) = \sin(\pi m x/L)\sin(\pi n y/L)$, where L is the size of the square membrane in the three resonances of the triplet. It is clear that all three eigenmodes are a mixture of all three basis functions and that the sign of the weight can be either positive or negative. This is not that surprising as the eigenmodes of mechanical systems are orthogonal to each other. This is clearly the case for the basis functions, but it can now also be tested for the measured mode shapes. After determining the weights w for the three resonances, these can be combined into a single matrix $W = [w_{\text{left}}, w_{\text{middle}}, w_{\text{right}}]$ and then the orthogonality of the modes is equivalent to having $W^{\mathrm{T}}W = \mathrm{I}$, where I is the 3 × 3 identity matrix.

Fig. 3(b) shows this product. It is clear that the diagonal elements are by far the largest. Although there are still non-zero off-diagonal elements, the product $W^{\mathrm{T}}W$ is indeed very close to I, confirming that the three resonances are close to orthogonal, something that is not at all trivial considering the complex mode shapes shown in the bottom row of Fig. 2. Future research will tell if this is also true when taking the in-product directly using the measured mode maps that is without first doing the modal projection.

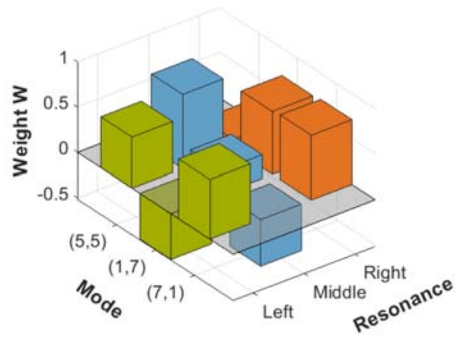

(a)

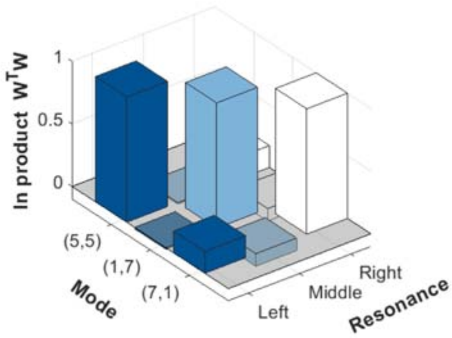

(b)

Fig. 3. (a) Weights W of the mode decomposition of the triplet (cf. bottom row of Fig. 2). The frequencies of the left, middle and right resonance were 7.3114, 7.3143, and 7.3180 MHz, respectively [2]. (b) Test of the orthogonality of the eigenmodes.

Looking back at the other modes in Fig. 2, shows that, although they are clearly identifiable, there are some small deviations from the expected mode shapes visible in the degenerate modes (1,2) and (2,1) as well as in (1,3) and (3,1). The question is, if these deviations are caused by mixing between the degenerate modes [15, 16]. Fig. 4 shows the results of the modal decomposition. The curved nodal lines are nicely reproduced in the fitted profiles. Looking at the weights shows that, in all cases, the largest weight is at the most prominent mode, but that for the degenerate modes, there is also a significant contribution from its partner. Such an analysis is important for the full understanding of, for example, mode competition in optomechanically-induced self-oscillating membranes [17].

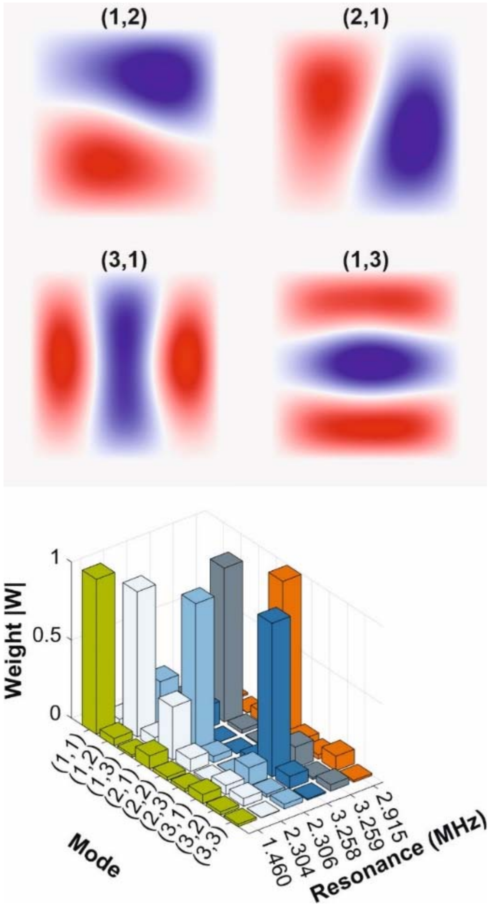

Fig. 4. Reconstructed mode maps (top) after linear fitting the measured mode maps of the degenerate (1,2), (2,1), (3,1) and (1,3) modes from Fig. 2 at 2.304, 2.306, 3.258, and 3.259 MHz respectively. The magnitude of the weights of the individual modes for the first six eigenmodes is shown in the bottom panel. In this case, the fitting is done for the 9 basis functions with $m,n = 1 .. 3$.

3. Mode Mapping in the Presence of Strong Crosstalk

The mode mapping method with the modified PLL works well for resonances in the low MHz range. However, when going to higher frequencies, e.g. by using smaller and thus stiffer resonators, a new challenge appears: the distortion of the resonances by crosstalk. The crosstalk is, in addition to the wanted mechanical excitation and transduction, a second pathway from excitation to detection. This is indicated by the orange line in the linear-system equivalent of the setup shown in Fig. 1(c). In our setup the crosstalk is electrical in nature. Although it does depend on frequency, when studying a single narrow resonance of the membrane, it can usually be considered constant and hence, instead of $X(\omega)$, its contribution is written as X.

In the Appendix, the origin of the crosstalk will be discussed in more detail, but it is clear that for a given amount of crosstalk, its effect becomes more pronounced when the mechanical signal is smaller. This can be due to many reasons, for example, a smaller membrane will have a higher spring constant; the same applies for a membrane with a larger mass. Also, the on-resonance mechanical signal is directly proportional to the quality factor [1], so an increase in dissipation will lead to smaller mechanical signals. Likewise, a reduction due to a lower readout efficiency (e.g. a film stack with less reflection), or a less efficient excitation of a particular mode will have a strong influence. Although hints of crosstalk were already present in our original work on that employed a large silicon nitride membrane with high quality factors [2], here its implications are studied on a different device: a smaller silicon nitride membrane that is covered by a layer of aluminum nitride [18, 19]. This device has a higher spring constant and, thus, higher fundamental resonance frequency and also lower quality factors. All of these factors make the impact of crosstalk much more severe. Still, such "sandwich" devices are instrumental in studying the mechanical properties of the AlN films [20].

Fig. 5 shows the driven response of this membrane in which several peaks, corresponding to the different out-of-plane vibrational modes, can be observed.

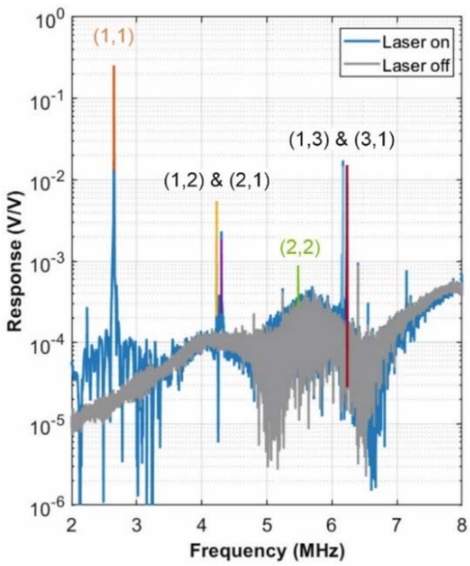

Fig. 5. Driven response of a 100×100 μm SiN membrane with ~ 210 nm aluminum nitride on top (blue). The gray line denotes the same measurement with the laser blocked, showing the crosstalk. The other colored lines show zooms that can be used to extract e.g. the exact resonance frequency or quality factors of the flexural modes.

For reference, the same measurement is repeated with the laser beam blocked (gray). In this case, there is no mechanical signal and only the crosstalk - as well as a few interference peaks - is visible. The labels indicate where the different modes are expected. From their position, the fundamental, i.e. (1,1), mode and the (2,2) mode can be identified unambiguously. The other visible low-lying modes, i.e. (1,2) & (2,1) and (1,3) & (3,1) of this square membrane are again expected to be degenerate and, although individual resonances are visible, their mode shape has to be imaged to identify them (or to obtain their weights in case of a linear combination). For this membrane, the fundamental mode is located at $f_{1,1}$ = 2.649 MHz, whereas for the silicon-nitride-only device shown in Fig. 2, this mode was at 1.460 MHz. This increase in the fundamental resonance frequency means that now the (2,2) mode is in the frequency range with the largest crosstalk as visible in the overview of the response shown in Fig. 5.

3.1. Resonances

Fig. 6 shows zooms of the driven response of the (2,2) mode of the AlN-covered membrane. One curve is measured with the network analyzer and the other one with the lockin amplifier. Although both the phase and amplitude response looks different, both show Fano-like resonances [21]. Considering the linear system equivalent of the measurement scheme as illustrated in Fig. 1(c), the resonances are fitted using the harmonic oscillator response functions with crosstalk included [11, 22, 23]:

$$Z(\omega) = z_{\mathrm{mech}} e^{i\alpha} \frac{\omega_0 \gamma}{\omega_0^2 - \omega^2 + i\omega\gamma} + z_X e^{i\phi_X} \quad (3)$$

From this, the mechanical and the crosstalk contributions are determined as summarized in Table 1.

Table 1. Values for the fit parameters for the data shown in Fig. 6. The uncertainty is 95 % confidence interval as given by MATLAB's fit function.

Param.	NWA	Lockin	
z_{mech}	0.499±0.003	0.455±0.003	mV/V
α	144.8±0.5	-21.8±0.5	deg.
z_X	0.19974±0.0013	0.2178±0.0013	mV/V
ϕ_X	132.7±0.4	125.4±0.4	deg.

The crosstalk z_X is similar in magnitude as the mechanical signal z_{mech} and the phase of the signal depends on which measurement device is used. This means that, although overview spectra, as e.g. in Fig. 5, are most efficiently acquired using the network analyzer, the parameters, such as setpoint and Z_{min} for the mode mapping, have to be determined from measurements with the lockin amplifier. It is noted that the lockin is expected to have a 2x lower signal as the two devices are connected in parallel. The lockin is set to high input impedance, whereas the network analyzer always has a 50 Ohm input impedance. This means that the load as seen by the low noise amplifier is 50 Ohm [24], but this has the consequence that the signal at the input of the lockin is reduced by a factor two compared to the case where the NWA was not connected.

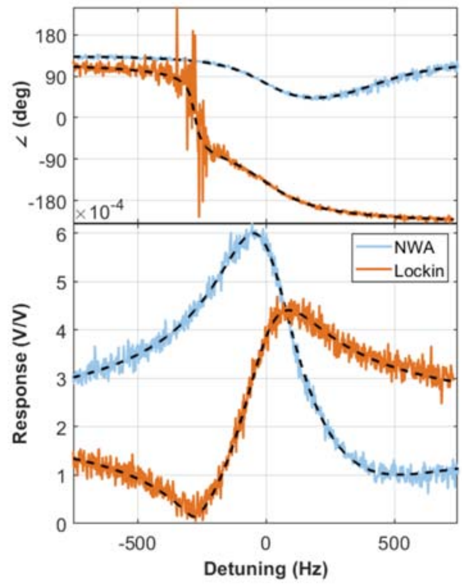

Fig. 6. Driven response of the (2, 2) mode measured with the network analyzer (NWA, blue) and the lockin amplifier (orange). The dashed lines are fits of Eq. (3) to the data; the fit parameters are listed in Table 1.

3.2. Implications for the PLL Operation

How exactly the crosstalk influences the PLL can be studied by taking the measured properties of the (2,2) mode (Table 1) and simulating what signal can be expected, how the PLL reacts to this, and what the resulting mode maps would look like. This is shown in Fig. 7. The top panels show the regular case, where no crosstalk is present. In this case, the phase at the resonance frequency takes two values that differ by exactly 180º or, equivalently, π rad. The modified PLL of Eq. (1) thus always locks to the resonance frequency for ϕ_{setpoint} = 0, and no frequency shift is observed (middle), i.e., Δf = 0. The resulting mode map will then accurately represent the actual mode profile. This is shown in the top right panel of Fig. 7.
The lower panels show that the situation is very different when the crosstalk is considered. The phase on resonance shows a smooth variation, taking any value between 0 and -180º. This means that at many points, the phase of the response at the resonance frequency is not that of the setpoint. The PLL will thus shift the driving frequency to accommodate this phase error. The lower middle panel shows the smallest possible Δf. It is clear that there are going to be large frequency shifts, exceeding the linewidth of the resonance. Also, the gray color indicates regions where there is no frequency for the PLL to lock to,

meaning that the driving frequency will keep on moving further and further from the resonance frequency. Note that the PLL improvement of only updating the frequency when the signal magnitude exceeds a threshold Z_{min} [cf. Eq. (2)], does not really solve this issue as z_X can be of the same order as the total signal Z, so that picking a suitable Z_{min} is difficult. Also note that due to the different phases between the mechanical and the crosstalk contributions, |Z| can be smaller than z_X, even when $z_{mech} \neq 0$. For a large part of the map, the PLL will not be able to lock close to the resonance frequency. This means that also the measured signal will be strongly affected. This is shown in the lower right panel of Fig. 7. Although the signature of the (2,2) can still be seen, it is clear that the map does not accurately represent the actual mode shape of the eigenmode. The presence of crosstalk is, thus, detrimental for mode mapping.

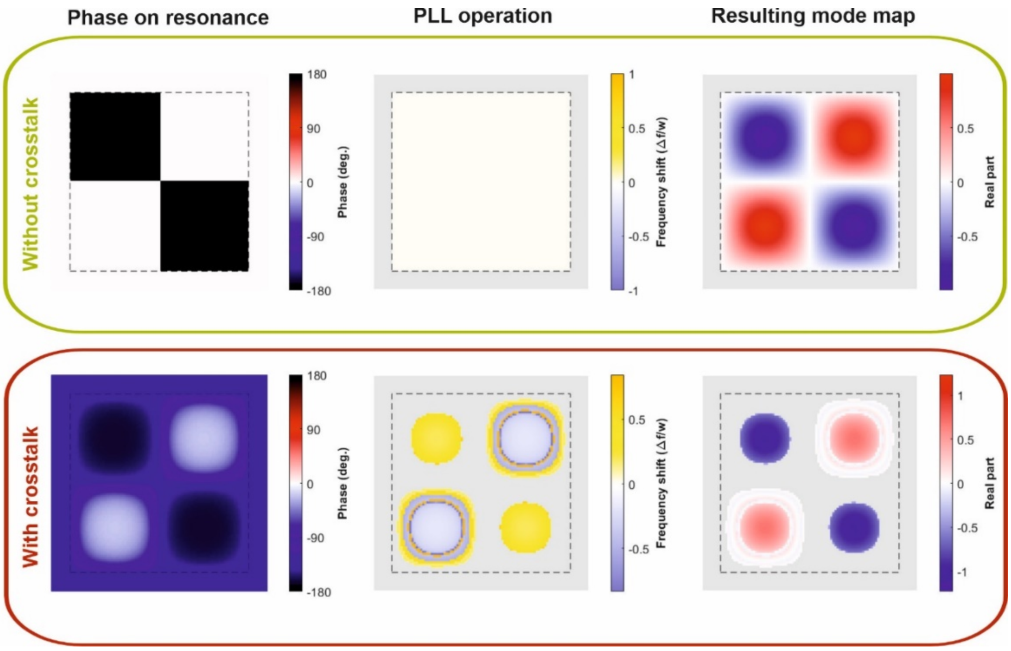

Fig. 7. Simulated operation of the PLL and mode mapping using parameters estimated for the (2,2) mode. The top row shows the expected signal without crosstalk, whereas the bottom row shows the same in the presence of crosstalk. The left panels are the phase of the signal at the resonance frequency. The middle panels show how much the frequency would shift when operating the modified PLL in units of the linewidth (full width of half maximum, FWHM) of the resonance. Gray indicates that the PLL cannot lock and will drift to large frequency shifts $|\Delta f| \gg w$. It is possible that there are no, or multiple frequencies where the signal has the setpoint phase. In the latter case, it is assumed that the PLL finds the frequency where the frequency shift is smallest. In practice the PLL may not find this value once it lost lock. The right panels show what the measured mode map would look like. In all panels, the dashed line indicates the outline of the square membrane.

3.3. Crosstalk Compensation and Maps

The good match of the fits of Eq. (3) to the data in Fig. 7 an d the correspondingly low uncertainty in the fit parameters (Table 1) give a first hint on how to solve the problem with crosstalk: If it is known well enough, it can be compensated for: Eq. (3) shows that the PLL should use $\angle\{Z - z_X^{est}\cdot\exp(i\phi_X^{est})\}$ instead of $\angle Z$ directly. If the estimation of the crosstalk is accurate, then

$$Z(\omega) - z_X^{\rm est} e^{i\phi_X^{\rm est}} \approx z_{\rm mech}(x,y) e^{i\alpha} \frac{\omega_0 \gamma}{\omega_0^2 - \omega^2 + i\omega\gamma} \quad (4)$$

which only contains the wanted mechanical part of the signal with its characteristic harmonic oscillator response, meaning that our modified PLL will operate regularly, i.e. as in the top panels of Fig. 6. The question is how well the crosstalk can be characterized beforehand. To study this, driven responses were acquired while scanning the sample underneath the focused laser spot [6]. Please note, that this is a lengthy procedure and is not advisable for high-resolution two-dimensional mode maps [2]. A number of representative traces, together with fits are shown in Fig. 8(a). By fitting all traces, the evolution of the fit parameters along the line scan can be determined. The plot in Fig. 8(b) shows that the mechanical contribution z_{mech} faithfully follows the mode profile (with some additional features due to the presence of the etching holes. [2]). On the other hand, z_X remains almost constant, as expected from the discussion at the beginning of Sec. 3. Next, the subtraction of the estimated (i.e. fitted) crosstalk from the data, as formalized by Eq. (4), is performed on the same three traces that were shown in Fig. 8(a). Fig. 9 shows that after this correction, the responses are now indeed the expected harmonic oscillator responses (dashed lines) and no longer show any sign of distorted Fano line shapes. Moreover, the phase of the gray curve is shifted by exactly 180 deg. compared to the other two, which is expected since Fig. 8(b) shows that that measurement was taken at the other side of the nodal line, where the mode profile changes sign. This shows the validity of the crosstalk-compensation approach. However, when taking a closer look at the results in Fig. 8(b), one notices that the fitted crosstalk is not entirely flat; some signatures of the mode shape (i.e. $\pm z_{\mathrm{mech}}$) can be seen in that line trace (Note that the fit uncertainty in both parameters is very small, see Table 1). At the moment, it is not clear where this comes from, but it is observed that:

1. The phase ϕ_X shows a similar "wiggle" as z_X;
2. There is no apparent structure in the residuals after the fit;
3. Fitting with a Duffing instead of a harmonic oscillator response does not change the outcome;
4. There is no y-dependence of the quality factor Q, nor of the phase α discernible;
5. The effect is also observed when using the NWA instead of the lockin, but with an opposite sign. This may be related to the difference in α between the two measurement devices (see Table 1).

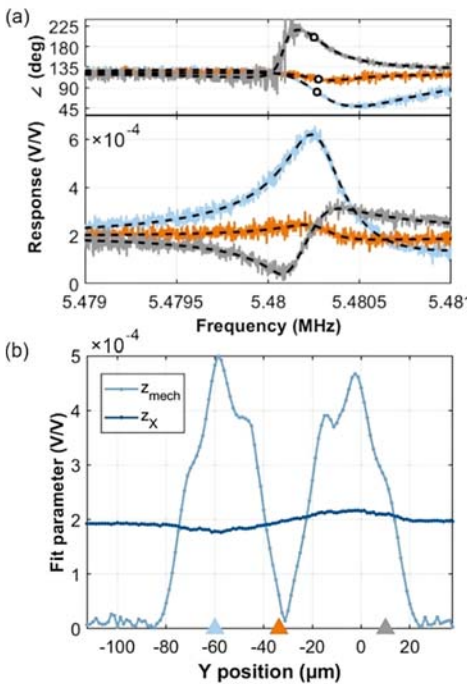

Fig. 8. (a) Measured frequency response (with the lockin) of the (2,2) mode at three different locations with fits using Eq. (3) (dashed lines). The circles indicate the phase ∠Z(ω₀); (b) extracted values for the mechanical and crosstalk contributions vs position on the membrane. The locations of the traces of (a) are indicated by the triangles.

Future checks, including considering the dynamic range of the different measurement devices and influence of the non-flat frequency response of the piezo shaker, will be done to solve this small riddle in the outcome of the fits. However, it turns out that it is not really necessary to first fit responses to obtain an accurate estimate for the crosstalk. As explained above, the crosstalk is electrical in nature and is also present when no light is detected. Hence, in practice, the signal is monitored for a while with the laser blocked and the PLL turned off. The mean of this signal is a good estimate for $z_X \cdot \exp(i\phi_X)$ and with this insight, the phase is locked successfully and mode maps are acquired. The result for the (2,2) mode is shown in Fig.10. It should be noted that the compensation of the crosstalk in the PLL is independent of the data acquisition and it can be decided afterward if this should be done, or not. First, panel (a) displays a map of the reflected laser power clearly showing the outline of the membrane with the supported parts in blue (low reflection) and the suspended part in red (high reflection). The etch holes are visible as the yellow spots in a square 7×7 lattice. Panel (b) shows the uncorrected mode map. The mode shape is already clearly visible, but the crosstalk still appears as a light blue background and the white nodal lines are not forming the cross shape expected for the (2,2) mode. After subtraction of the crosstalk, the mode map in panel (c) is obtained. There, it is clearly visible that now there are the expected straight nodal lines (in white) and equal amplitudes of the anti-nodes. Of course, since this measurement is done on a smaller membrane with a lower quality factor ($Q_{2,2}$ = 17547±18 corresponding to a FWHM of 312.3±0.3 Hz) compared to our earlier work [2], one may think that no frequency shifts have happened during its acquisition, but this is not the case. Fig. 10(d) shows the frequency shift that the PLL has corrected. In this case, shifts of the order as the FWHM of the resonance are observed, indicating that even in this case it is necessary to do the mode mapping while the PLL tracks the resonance frequency.

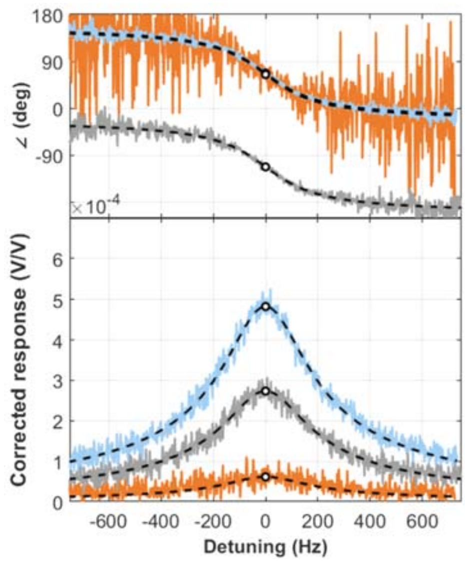

Fig. 9. Responses of Fig. 8 (a) after subtracting the fitted crosstalk. The dashed lines are harmonic oscillator response functions. The circles indicate the values at the resonance frequency.

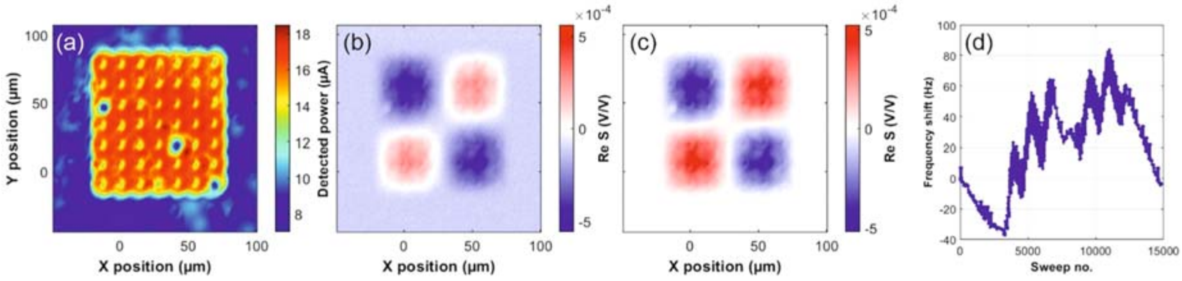

Fig. 10. Measured map of the (2,2) mode with crosstalk compensation in the PLL. (a) Reflected laser power as detected using the a Keithley 485 picoamp meter connected to the photo detector. Mode maps before (b) and after (c) crosstalk subtraction. (d) Evolution of the driving frequency during the measurement as updated by the modified PLL with crosstalk subtracted.

5. Conclusions

A powerful method to visualize the eigenmodes of mechanical resonators is demonstrated. It is shown that with the modified PLL, modes with regions without a strong response or with sign changes can be mapped, and that this can be used to quantitatively analyze the mode profiles. Here, we demonstrated this with the decomposition of a triplet mode, the orthogonality of these modes, as well as the mixing of the (1,2) and (2,1) modes.

Especially for stiffer membranes, crosstalk becomes apparent. With experimental parameters, the operation of the PLL is simulated and it is shown that crosstalk is detrimental for the operation of the mode mapping method. By determining the crosstalk accurately, its effect can be subtracted from the measured signal, enabling again the operation of the (modified) PLL. This means that now even in the presence of strong crosstalk accurate mode maps can be obtained.

Acknowledgements

This work was presented during the OPAL-2022 conference and we thank the participants for the discussions and constructive questions, some of which have found their way into this paper. The research was funded by the German Research Foundation (DFG) [EXC-2111-390814868] and TUM-IAS, funded by the German Excellence Initiative and the European Union Seventh Framework Programme [grant agreement 291763]. We thank X. Yao for assistance with the nanofabrication, and L. Rosendahl and E. Lebedev for help with the setup and measurements.

References

[1]. M. Poot and H. S. J. van der Zant, Mechanical systems in the quantum regime, *Phys. Rep.*, Vol. 511, 2012, p. 273–335.

[2]. D. Hoch, K.-J. Haas, L. Moller, T. Sommer, P. Soubelet, J. J. Finley and M. Poot, Efficient Optomechanical Mode-Shape Mapping of Micromechanical Devices, *Micromachines*, Vol. 12, July 2021, p. 880.

[3]. D. Hoch, K.-J. Haas, L. Moller, J. Röwe, T. Sommer, P. Soubelet, J. J. Finley and M. Poot, Efficient Optomechanical Mode-Shape Mapping of Micromechanical Devices in the Presence of Crosstalk, in *Proceedings of the 5th International Conference on Optics, Photonics and Lasers (OPAL' 2022)*, Spain, 2022, pp. 32-33.

[4]. A. Barg, Y. Tsaturyan, E. Belhage, W. H. P. Nielsen, C. B. Møller and A. Schliesser, Measuring and imaging nanomechanical motion with laser light, *Applied Physics B,* Vol. 123, 2016, p. 8.

[5]. X. Zhang, R. Waitz, F. Yang, C. Lutz, P. Angelova, A. Gölzhäuser and E. Scheer, Vibrational modes of ultrathin carbon nanomembrane mechanical resonators, *Appl Phys Lett,* Vol. 106, 2015, 063107.

[6]. D. Davidovikj, J. J. Slim, S. J. Cartamil-Bueno, H. S. J. van der Zant, P. G. Steeneken and W. J. Venstra, Visualizing the Motion of Graphene Nanodrums, *Nano Lett.,* Vol. 16, April 2016, p. 2768–2773.

[7]. Z. Shen, X. Han, C.-L. Zou and H. X. Tang, Phase sensitive imaging of 10 GHz vibrations in an AlN microdisk resonator, *Review of Scientific Instruments*, Vol. 88, December 2017, 123709.

[8]. E. Romero, R. Kalra, N. P. Mauranyapin, C. G. Baker, C. Meng and W. P. Bowen, Propagation and Imaging of Mechanical Waves in a Highly Stressed Single-Mode Acoustic Waveguide, *Phys. Rev. Applied*, Vol. 11, No. 6, June 2019, p. 064035.

[9]. R. Singh and T. P. Purdy, Detecting Acoustic Blackbody Radiation with an Optomechanical Antenna, *Phys. Rev. Lett.,* Vol. 125, No. 12, September 2020, p. 120603.

[10]. T. Hesjedal, E. Chilla and H.-J. Fröhlich, High resolution visualization of acoustic wave fields within surface acoustic wave devices, *Appl Phys Lett*, Vol. 70, 1997, pp. 1372-1374.

[11]. S. Etaki, M. Poot, I. Mahboob, K. Onomitsu, H. Yamaguchi and H. S. J. van der Zant, Motion detection of a micromechanical resonator embedded in a d.c. SQUID, *Nature Physics*, Vol. 4, October 2008, p. 785–788.

[12]. D. Garcia-Sanchez, A. S. Paulo, M. J. Esplandiu, F. Perez-Murano, L. Forró, A. Aguasca and A. Bachtold, Mechanical Detection of Carbon Nanotube Resonator Vibrations, *Phys. Rev. Lett.*, Vol. 99, 2007, p. 085501.

[13]. D. Garcia-Sanchez, A. M. van der Zande, A. S. Paulo, B. Lassagne, P. L. McEuen and A. Bachtold, Imaging Mechanical Vibrations in Suspended

Graphene Sheets, *Nano Letters,* Vol. 8, May 2008, p. 1399–1403.
[14]. K. S. Shanmugan and A. M. Breipohl, Random signals: detection, estimation and data analysis, *John Wiley & Sons*, 1988.
[15]. J.-H. Kang and B. Wei, Degenerate mode shapes for rectangular membranes and simply supported rectangular plates, *Journal of Vibration and Control,* Vol. 21, August 2013, p. 1633–1638.
[16]. S. Chakram, Y. Patil, L. Chang and M. Vengalattore, Dissipation in Ultrahigh Quality Factor SiN Membrane Resonators, *Physical Review Letters*, Vol. 112, March 2014, p. 127201.
[17]. U. Kemiktarak, M. Durand, M. Metcalfe and J. Lawall, Mode Competition and Anomalous Cooling in a Multimode Phonon Laser, *Physical Review Letters*, Vol. 113, July 2014, p. 030802.
[18]. G. Terrasanta, M. Müller, T. Sommer, S. Geprägs, R. Gross, M. Althammer and M. Poot, Growth of aluminum nitride on a silicon nitride substrate for hybrid photonic circuits, *Materials for Quantum Technology,* Vol. 1, June 2021, p. 021002.
[19]. G. Terrasanta, T. Sommer, M. Müller, M. Althammer, R. Gross and M. Poot, Aluminum nitride integration on silicon nitride photonic circuits: a hybrid approach towards on-chip nonlinear optics, *Optics Express*, Vol. 30, March 2022, p. 8537.
[20]. A. Yadav, Optomechanics on a Chip, 2022.
[21]. U. Fano, Effects of Configuration Interaction on Intensities and Phase Shifts, *Physical Review,* Vol. 124, December 1961, p. 1866–1878.
[22]. D. Hoch, X. Yao and M. Poot, Geometric Tuning of Stress in Predisplaced Silicon Nitride Resonators, *Nano Lett*., Vol. 22, May 2022, pp. 4013-4019.
[23]. M. Poot, S. Etaki, H. Yamaguchi and H. S. J. van der Zant, Discrete-time quadrature feedback cooling of a radio-frequency mechanical resonator, *Appl Phys Lett,* Vol. 99, July 2011, p. 013113.
[24]. P. Horowitz and W. Hill, The art of electronics, 3rd ed., *Cambridge University Press*, 2015, p. 1224.
[25]. M. Poot, K. Y. Fong and H. X. Tang, Deep feedback-stabilized parametric squeezing in an opto-electromechanical system, *New J Phys*, Vol. 17, 2015, p. 043056.

Appendix. Origin of the Crosstalk in the Setup

Although it is thus possible to correct for the crosstalk, both in the operation of the PLL, as well as in the measured signal using the method presented in this work, so far it has not been discussed what the origin of the crosstalk is. To investigate this, the driven response of the (2,2) mode is measured repeatedly at the same location on the membrane, while systematically changing certain aspects of the setup. From the fits of the driven response, both the magnitude (and phase) of the crosstalk and the mechanical signal are determined. This way, it can be studies how changes to the setup impact these contributions. The results are listed in Table 2.

These indicate that, as expected, the mechanical signal is proportional to the laser power and the total gain. Hence, any attenuation will reduce its magnitude and it vanishes when there is a blocking anywhere. For the crosstalk the situation is more complex. Here, the amount of light is (1-4) is irrelevant, but small changes to the electrical connections in the setup that at first may seem irrelevant (5, 6) change the amount of crosstalk. The crosstalk does not originate in the lockin itself (9) but is present in all other measurements. It is amplified by the amplifier and thus affected by its gain (8) or when its magnitude is reduced before the amplifier (9). However, even when e.g. disconnecting the cable to the piezo, there is still a significant amount of crosstalk present. In this case, the pathway must have gone via the combiner and the network analyzer. However, even when the latter was disconnected (5), crosstalk was not eliminated (actually an increase was observed). All these measurements confirm that the crosstalk is electrical in nature and hints that there are several parallel pathways that cause the total crosstalk, as was indicated by the dashed lines in the schematic of setup in Fig. 1(c). The increase in crosstalk with frequency that is visible in Fig. 5 (gray curve) is consistent with both a capacitive and as well as an inductive coupling.

Table 2. Measurements of the crosstalk and peak mechanical contribution when varying the measurement conditions and changing the measurement setup. The symbols =, ↓, ⇓, 0, and ~ indicate, respectively, that the parameter did not vary compared to the regular measurement, that is was lower, that is was more than an order of magnitude lower, that it was 0, or different but similar in magnitude. All measurements were taken with the lockin amplifier.

No.	Description	z_X	z_{mech}
1.	Regular measurement	=	=
2.	Reduce laser power	=	↓
3.	Laser blocked	=	0
4.	Detector blocked	=	0
5.	Disconnect NWA (replace by 50 Ω terminator)	~	=
6.	Disconnect pA meter (replace by 50 Ω terminator)	~	=
7.	Disconnect photo detector	↓	0
8.	Amplifier off (but still connected)	⇓	0
9.	6 dB attenuation before amp	↓	↓
10.	Disconnect lockin output	0	0
11.	Disconnect cable to piezo	↓	0

Sensors & Transducers, Vol. 258, Issue 4, July 2022, pp. 10-17

Sensors & Transducers
Published by IFSA Publishing, S. L., 2022
http://www.sensorsportal.com

Terahertz Optoelectronic Devices Based on Three-Dimensional Modelling of Symmetrically Coupled Surface Plasmon Polariton Resonances in Bulk Dirac Semimetal

[1] Tony Mathew Blessan, [2] M. Gayathri, [2] T. Alagesan, [1, 3*] N. Yogesh
[1] Department of Nuclear Physics, University of Madras (Guindy Campus), Chennai -600025, India
[2] Department of Physics, Presidency College, Chennai 600005, India
[3] Department of Physics, National Institute of Technology (Calicut), Kerala -673601, India
E-mail: yogesh@nitc.ac.in

Received: 20 June 2022 /Accepted: 22 July 2022 /Published: 29 July 2022

Abstract: Bulk Dirac Semimetal (BDS) - a three-dimensional counterpart of graphene, prominently known for its topologically protected linear dispersion energy bands embraces remarkable plasmonic responses at terahertz (THz) frequencies, which can be well capitalized for its optoelectronic applications. Recently, we have demonstrated the BDS based THz plasmonic applications such as surface plasmon polariton assisted microparticle sensing, THz waveguiding with curved/bending geometries and all-optical THz logic gates. However, all of the demonstrations were restricted with 2-D BDS geometries where height of the BDS was assumed to be infinity. For practical applications, it is essential to consider the height dimension in device realization. In this work, we demonstrate 3-D numerical modelling results of BDS based THz applications by considering height dimension of the BDS in the design of curved waveguides, sub-wavelength waveguiding in tapered geometries and 3-D XOR logic gate. We anticipate that the above findings manifest BDS as a potential candidate for opening new avenues in the realization of THz optoelectronic devices.

Keywords: Bulk Dirac semimetal (BDS), Sub-wavelength waveguiding, THz logic gate, 3-Dimensional, Surface plasmon polariton (SPP).

1. Introduction

Photonic circuits having high operating speed faces the challenge of critical low dimension sizes whereas electronic circuits in nanometer scales have very low operating speed. Therefore, achieving a circuitry device with sub-diffraction dimension and high operational speed is of prime importance. Hence, an optoelectronic integrated circuit that provides enhanced operational speed, low power consumption and reduced interconnect delay in optical communications is highly warranted [1]. One of the key technologies to realize optoelectronic integrated circuit in 3-D geometries is plasmonics [2]. Surface Plasmon Polariton (SPP) are the quanta of quasi-interaction between electromagnetic (e-m) wave and plasmons (collective excitations of electrons) at the interface between plasmonic material and a dielectric [3]. This light-matter interaction is best suited for miniaturized photonic circuits due to its sub-wavelength features [4, 5]. At optical frequencies, bulk metals show negative dielectric permittivity and they exhibit plasmonic response [6]. However, extending conventional metals such as Au, Ag and Cu to excite SPP in THz regime is a cumbersome task as Lorentz-Drude model predicts a high value of imaginary dielectric permittivity (ε_r'') [7]. The availability of natural materials with plasmonic response is also limited in the THz range (0.1 THz -10 THz). It is to be mentioned that various different techniques such as periodic metal gratings [8] and artificial materials like metamaterials, graphene [9] are also employed for THz plasmonic applications.

In the past few years, relativistic fermions were found to be emerged as low-energy excitations in materials known as Dirac semimetals [10]. Therefore, researchers are exploring the option of employing bulk Dirac semimetals (BDS) such as Cd_3As_2 [11], Na_3Bi and $ZrTe_5$ for SPP interaction in the THz regime. In a typical BDS, electronic states are extended in all three dimensions and therefore one can expect 3-D Dirac points (point at which valence and conduction bands meets) instead of 1-D Dirac points as in the case of graphene. Due to 3-D extension of dispersion in BDS, carrier mobility in BDS is very high [12–15] and this unique bandstructure constitutes BDS as a suitable material for optoelectronic applications at THz waveband [16-19].

In our previous study, we have reported how the curved geometries of BDS sustain THz SPPs using Kretschmann–Raether and Otto configurations [20]. Moreover, in our latest report we also demonstrated the possibility of SPP waveguiding and all optical THz logical gates with BDS [21]. However, BDS were treated as 2-D geometries, in which height of the BDS was taken to be infinity. For practical consideration, one needs to take care of the height dimensions. In this work, we have performed 3-D numerical simulation with BDS for THz waveguiding in straight and curved geometries so that reliability of the results is not only validated, but also, we have attained a step towards device prototypes for novel THz optoelectronic applications. By exciting symmetrically coupled SPP in multilayer BDS, two different 3-D tapered geometries for sub-wavelength waveguiding are demonstrated in this work. Furthermore, a simple Y structured geometry for the functioning of THz plasmonic gate (XOR) is illustrated with the idea of integrating BDS with photonic circuits.

2. Bulk Dirac Semimetal

The Dirac semimetal is an unusual material in which the nodes of the bulk electronic states are protected against the gap formation by crystalline symmetry leading to high carrier mobility and dramatically reduced intrinsic Ohmic losses. We observe that BDS is a promising candidate for THz plasmonic applications in the regime (0.5 THz – 2 THz) by theoretically analyzing its dielectric response. The dielectric response of a BDS is expressed as $\varepsilon_r(\omega) = \varepsilon_\infty + \frac{i\sigma(\omega)}{\omega\varepsilon_0}$ where $\varepsilon_\infty = 13$, ε_0 is the permittivity of vacuum and conductivity $\sigma(\omega)$ is obtained from Kubo formalism as

$$\sigma(\omega) = \frac{ie^2}{\hbar}\frac{g_1}{6\pi^2 v_F \hbar^2}\frac{\mu_c^2 + \frac{(k_B T)^2}{3}}{(\omega + i\tau^{-1})}$$

where $T = 300$ K is the temperature, $\tau = 1.2$ ps is the relaxation time, k_B is the Boltzmann constant, $v_F = 0.9\times10^6\, ms^{-1}$ is the Fermi velocity, $g_1 = 4$ is the degeneracy factor and $\mu_c = 0.1\ eV$ is the chemical potential [22]. At lower THz regime, intraband conductivity dominates and thus contribute to the SPP formation, and hence the interband conductivity has not been taken into account in $\sigma(\omega)$ equation mentioned above.

One striking advantage of BDS is its tunability and it is usually achieved by varying the Fermi energy that can in turn alter the dielectric permittivity of BDS. To what extent the Fermi energy can be varied at room temperature (such that linear dispersion of energy band still holds) is a question of experimental analysis. However, under low temperature and long wavelength limit, theoretically the E_F can be varied from 0.03 eV – 0.15 eV in order to maintain the linear dispersion regime. Additionally, it is noteworthy to mention that relaxation time of charge carriers in BDS also plays an important role in the dielectric permittivity of BDS. Fig. 1(a) shows the dielectric permittivity of BDS at E_F = 0.1 eV for above mentioned parameters. Fig. 1(b) is plotted for three varying E_F as 0.06 eV, 0.10 eV and 0.14 eV. Fig. 1(c) emphasizes how the relaxation time influences the dielectric permittivity of BDS when $\tau_s = 0.157$ ps (experimental reference [23]) and $\tau_s = 1.2$ ps. One can infer from Fig. 1(a) that BDS is an excellent candidate for supporting SPP in 0.1 THz – 2 THz regime because the imaginary part of ε_r is considerably small. To comprehend it, as an example one can witness from Table 1 and 2 how Fermi energy and relaxation time manifest dielectric response of BDS at f = 0.9 THz. This frequency is chosen for demonstrative purposes. However, one can chose any value from 0.1 – 2 THz.

All the numerical simulations performed in this work are performed at E_f = 0.1 eV and τ_s = 1.2 ps.

Table 1. E_f vs ε_r at f = 0.9 THz and τ_s = 1.2 ps.

Fermi Energy E_f (eV)	ε_r'	ε_r''
0.06	- 555.2	81.83
0.10	- 1485	218.8
0.14	- 2880	424.3

Table 2. τ_s vs ε_r at f = 0.9 THz and E_f = 0.1eV.

Relaxation Time τ_s (ps)	ε_r'	ε_r''
0.157 [23]	-657.9	755.7
1.2	-1477	219.6

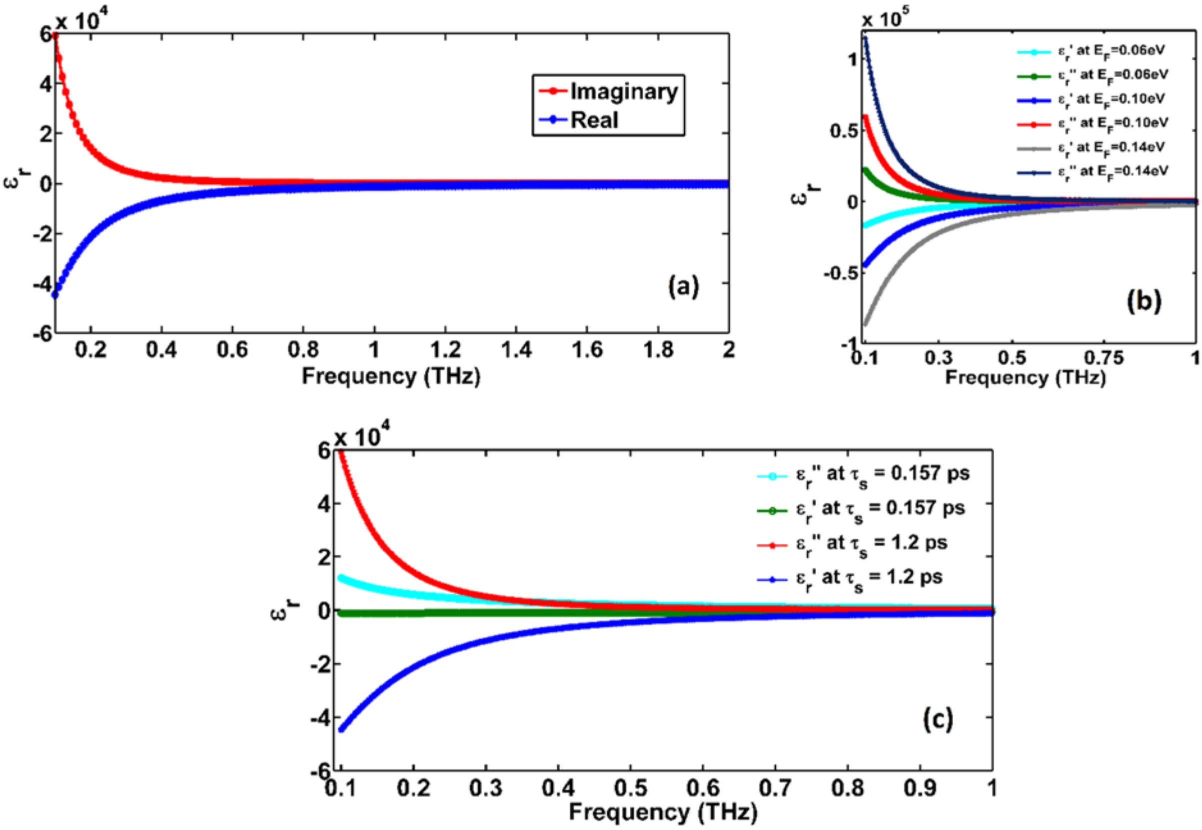

Fig. 1. a) Dielectric permittivity of BDS at E_f = 0.1 eV and τ_s = 1.2 ps; b) varying E_f at τ_s = 1.2 ps; c) varying τ_s at E_f = 0.1 eV.

3. THz SPP Waveguiding in 3-D Curved BDS Geometry

One of the main limitations in guiding geometries are the radiation leakages along sharp bends and corners. Here we demonstrate how SPP in BDS can overcome the issue of losses along corners and bends. It is known that when the separation between two adjacent BDS sheets is smaller than the skin depth, SPP at each BDS boundaries can interact together to form a coupled propagating (symmetric or anti-symmetric) SPP mode. In our previous work [20, 21], detailed analysis of THz SPP sustainment in single and multilayer BDS curved geometries have been examined. In order to deduce whether anti-symmetric or symmetric mode SPP is most suitable for long range waveguiding, eigen mode analysis were performed in single and multilayer BDS geometries. It was found that the real part of the wave vector ($\mathrm{Re}(\beta)$) of the symmetric mode is higher than anti-symmetric mode and this concluded why symmetrically coupled THz SPP mode are preferred over anti-symmetric SPP mode [21]. Here we extent our analysis to 3-D BDS geometries. Firstly, BDS-Air-BDS multilayer with optimized air gap (***g***) of 50 μm between two BDS slabs of height 850 μm and optimized thickness of 7 μm (shown in Fig. 2(a)) is modelled with scattering boundary conditions in all three directions and solved using COMSOL RF module [24] with boundary mode analysis. The choice of BDS height after optimization is taken as 850 μm with the aim that there is minimum amount of transmission losses. Using industrial chemical vapor deposition technique and 3-D laser printing one can coat BDS over a large area substrate and therefore the choice of 850 μm height for BDS sheet may be possible to realize in near future. The H_z field profile at 1.9 THz given in Fig. 2(b) shows the sustainment of SPP mode in BDS parallel waveguide. When a perturbation is introduced in the form of a macrobend (radius of curvature is 500 μm) as shown in Fig. 2(c), SPP still sustained along the bend. At f =1.9 THz, the S_{21} for straight and curved BDS is 93.67 % and 91.32 % respectively. For a curved geometry with radius of curvature 500 μm, the transmission loss is negligible (~0.0235 %) when compared to straight geometry and the corresponding H_z field profile at 1.9 THz given in Fig. 2(d) ascertains that symmetric SPP can evade bends efficiently without much losses, as SPP is confined within the BDS walls.

4. Sub-wavelength THz SPP Waveguiding

The control of electromagnetic wave at sub-wavelength scale for channeling light in fibre-optics and surface-wave waveguides are of great interest among researchers [25]. Our earlier work analysed how tapered geometries in 2-D support symmetrically coupled SPP mode within BDS walls where aperture miniaturization of $\sim\frac{\lambda}{6}$ were achieved [21]. Here we extend the 2-D geometry in order to understand the cut off dimension for the tapered geometry in which the coupling from high aperture to low aperture is controlled by gradually reducing the separation gap ($\boldsymbol{g}$) between the BDS film. Fig. 3(a) shows a parallel BDS waveguide with dimensions $50\ \mu m \times 300\ \mu m$ tapered to a width of $80\ \mu m$ on both input and output. The corresponding transmission plot in Fig. 3(b) shows that the THz beam propagation is allowed in tapered geometry with above 83% transmission efficiency for the range of 0.85 THz - 2 THz. The inset in Fig. 3(b) shows the H_z field map at f = 1 THz exhibiting sub-wavelength behavior. However, when the dimension of BDS waveguide is reduced to $1\ \mu m \times 300\ \mu m$ with the tapering geometry dimension of $80\ \mu m$ as shown in Fig. 3(c), all frequencies from 0.85 THz – 2 THz are completely forbidden which is evident from the S_{21} plot (Fig. 3(d)) and H_z field map at f = 1 THz (inset of Fig. 3(d)). This indicates that the tapered geometry has a cut off at $\boldsymbol{g} = 1\ \mu m$. It is noteworthy to mention here that the cut off characteristics has been studied with 2-D BDS geometries. Because retrieving S_{21} parameter for a large range of frequencies is cumbersome for 3-D case. Nevertheless, we try to solve field map for a particular frequency proficiently in 3-D geometry by choosing a single frequency from the S_{21} plot of 2-D geometry. Two different tapered 3-D geometries are modelled for studying the sub-wavelength guiding of BDS waveguide. In Fig. 4(a), an air-filled perfect magnetic conducting (PMC, $\hat{n} \times \vec{H} = \vec{0}$) waveguide of dimension $300\ \mu m \times 50\ \mu m \times 850\ \mu m$ is connected with two tapered geometries with dimension of $350\ \mu m \times 80\ \mu m \times 850\ \mu m$ at both input and output interfaces. As a support, SiO_2 substrate ($\varepsilon_r = 4.2$) of dimension $1020\ \mu m \times 600\ \mu m \times 50\ \mu m$ is placed at the bottom. In Fig. 4(b), H_z field pattern at 1 THz shows that PMC tapered waveguide does not allow beam to pass through it. However, in case of parallel BDS waveguide of same dimensions shown in Fig. 5(a), THz beam propagation is allowed with 96 % transmission at f = 1 THz. The field pattern given in Fig. 5(b) at 1 THz reveals sub-wavelength guiding behaviour of multilayer BDS system.

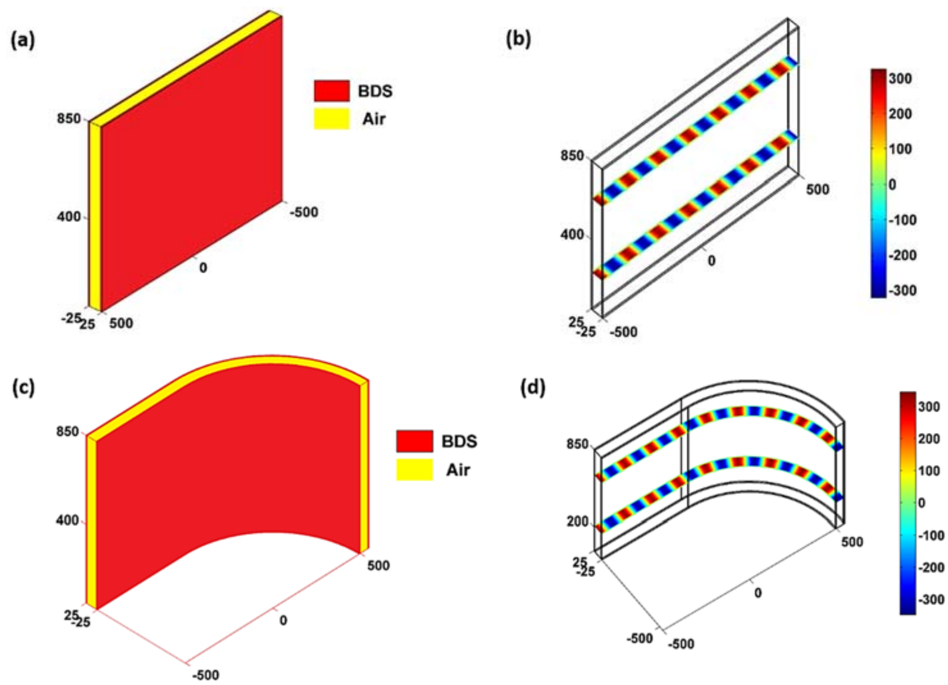

Fig. 2. BDS-Air-BDS configuration a) Straight 3-D geometry; b) H_z field map at 1.9 THz in straight geometry; c) Macro bend 3-D geometry; d) H_z field map at 1.9 THz in macro bend 3-D geometry.

Apart from tapered geometry, we have also tested whether any shape of BDS waveguide sustains SPP confinement. For this purpose, an arch of radius 500 μm and 50 μm × 850 μm dimension is designed with two tapered geometries with dimension 437 μm × 80 μm × 850 μm at both input and output interfaces as shown in Fig. 6(a). To support the configuration, SiO_2 substrate ($\varepsilon_r = 4.2$) of dimension $2010\ \mu m \times 700\ \mu m \times 50\ \mu m$ is placed at the bottom. In order to see the response of arch geometry, initially S_{21} plot is obtained for 2-D geometry. As the arch geometry is a semicircle of resonating nature, one expects periodic dip in S_{21} plot and it is evident from

Fig. 5(b). From S_{21}, two frequencies are chosen such that one frequency is allowed and other is prohibited and these two specific frequencies are solved in 3-D geometry. H_z field pattern in Fig. 5(c) corresponds to f = 0.948 THz in which maximum transmission efficiency of more than 85 % is observed and in Fig. 5(d) H_z profile at 1.152 THz is given, where transmission efficiency is observed to be less than 48%. Hence, from the above results it is clear that coupled SPP modes can be guided for any tapered geometry with good efficiency for larger bandwidth.

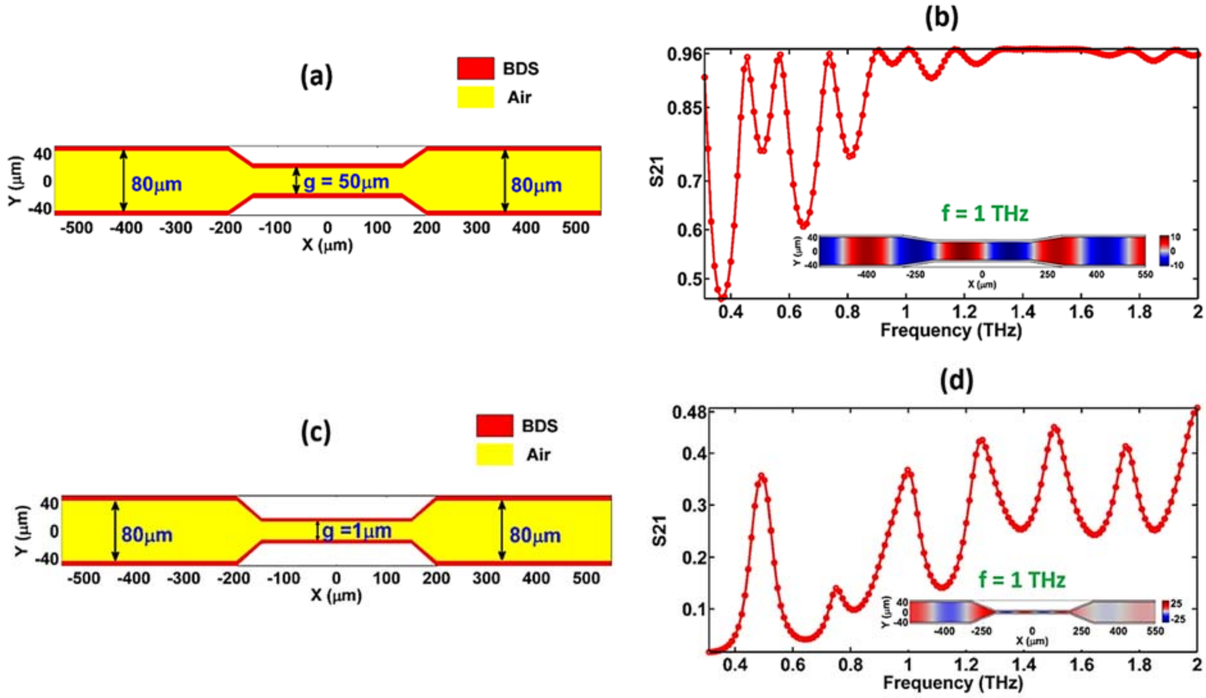

Fig. 3. (a) 2-D geometry of tapered multilayered BDS waveguide of 50 µm; (b) corresponding transmission plot and H_z field at 1 THz shown in the inset; (c) 2-D geometry of tapered multilayered BDS waveguide of 1µm; (d) corresponding transmission plot and H_z field at 1 THz is shown in the inset.

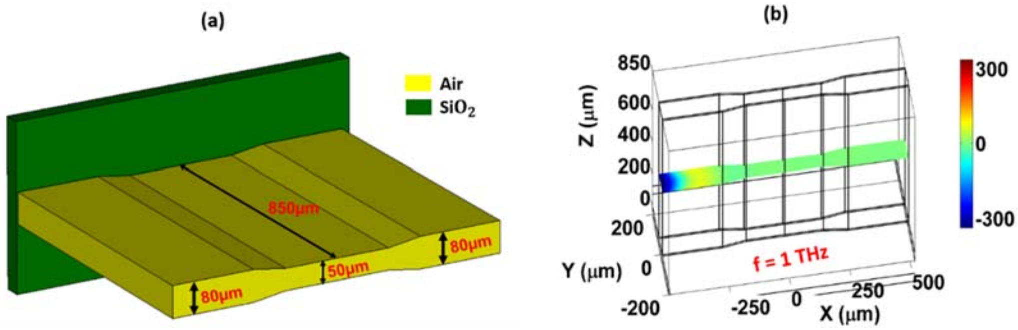

Fig. 4. (a) 3-D geometry of air filled PMC waveguide; (b) H_z field map of 3-D geometry at 1 THz.

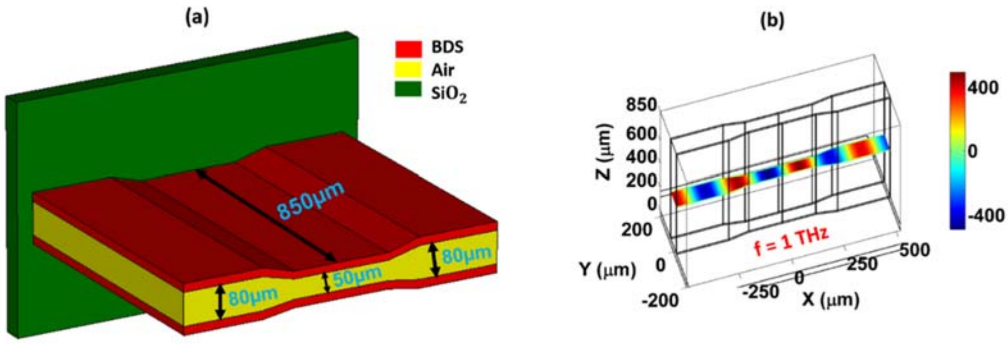

Fig. 5. (a) 3-D geometry of multilayer BDS waveguide; (b) H_z field map of 3-D geometry at 1 THz.

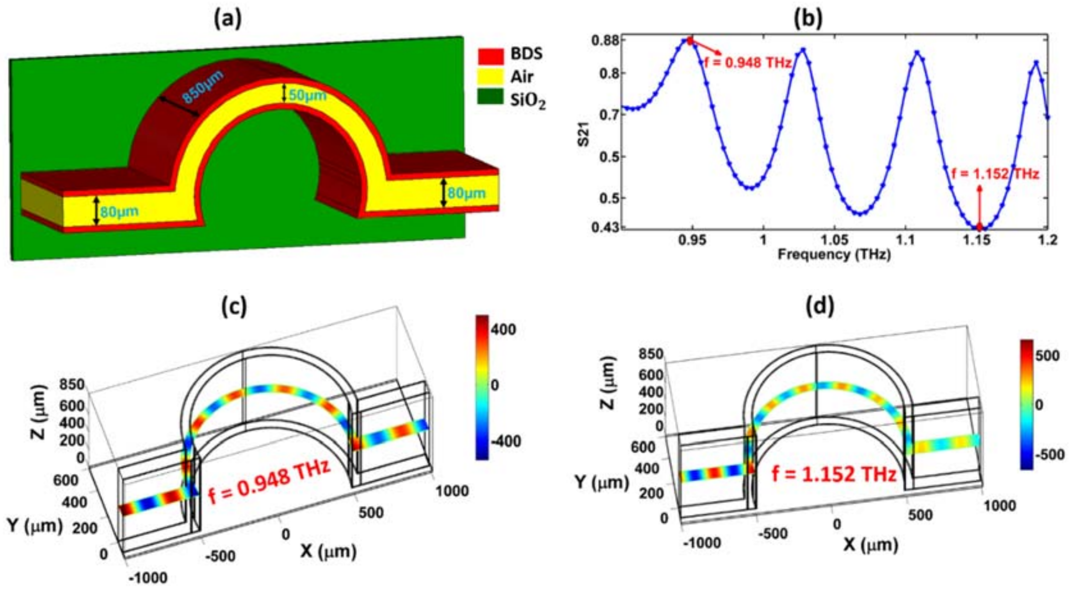

Fig. 6. (a) 3-D geometry of multilayered BDS arch waveguide; (b) transmission plot obtained from 2-D arch geometry, and (c) and (d) H_z field map at 0.948 and 1.152 THz for 3-D arch geometry.

5. Plasmonic Terahertz Logic Gates

Logic gates have potential applications especially in the field of information processing because of its high speed performance with minimum power consumption. They serve as basic components of an optical signal processing system and act as a bridge between electrical and optical calculations [26]. Various research groups have achieved logic gates using metamaterials [27] and photonic crystals [28]. One notable contribution was in developing sub-wavelength graphene-based plasmonic 3-D waveguide that performs THz AND/OR logic gate [29]. In this section, the waveguiding feature (Fig. 2) shown already in parallel BDS system with circuit miniaturization can be extended to the realization of logic gates as it is an essential component for the empowerment of THz optoelectronics. Considering the evading nature of symmetric mode SPP in macro bend geometry, one can very well reach out its application to logic gate. Fig. 7(a) shows the geometry of XOR gate in the form of Y-structure whose input arms are separated by 136 µm and the continuing arm of length 600 µm serves as an output. When symmetric coupled SPP modes in each input arm are in phase with each other, constructive interference occurs and when they are 180° out of phase with each other, destructive interference takes place which cancels out the output signal in the detection port. To support the Y configuration, SiO_2 substrate ($\varepsilon_r = 4.2$) of dimension $1500\ \mu m \times 600\ \mu m \times 50\ \mu m$ is placed at the bottom. The norm of magnetic field strength ($|\vec{H}|$) patterns shown in Fig. 4(b), 4(c) and 4(d) demonstrate XOR gate at frequency 1.192 THz. The output transmission level less than 50 % can be marked as a threshold for OFF state. Interestingly, the destructive interference of coupled SPP modes corresponds to low transmission level of 15.60 % at 1.192 THz. Table 3 shows the truth table for XOR gate at 1.192 THz.

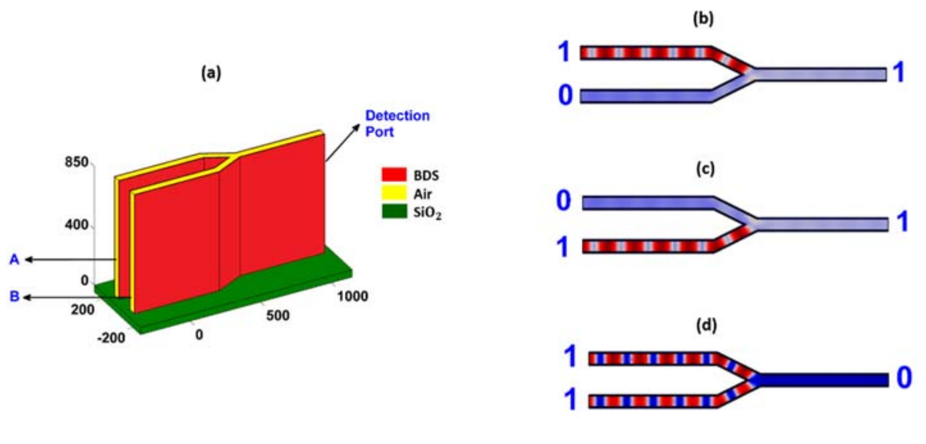

Fig. 7. (a) 3-D logic gate design formed by parallel BDS structure; (b) - (d) represent norm of $\vec{H}$ field patterns for XOR at 1.192 THz.

Table 3. Truth table for XOR gate.

Input		Output (S21%)
A	**B**	**XOR (1.192 THz)**
0	0	0
1	0	62.90
0	1	62.91
1	1	15.60

6. Conclusions

To conclude, 3-D modelling of BDS multilayer system in straight and bending geometries were studied. By exploiting coupled SPP modes, subwavelength THz waveguiding in two different tapered geometries were illustrated. A 3D THz XOR logic gate has been successfully demonstrated by utilizing the interference nature of SPP. The above reported 3D waveguide, logic gate and along with the advent of operating room temperature BDS [24, 30], we believe that designing BDS based THz optoelectronics devices will open new horizon on chip scale circuitry levels.

Acknowledgements

This work was done based on the facilities funded by the Department of Science and Technology, Ministry of Science and Technology, India (DST/INSPIRE/04/ 2015/002420).

References

[1]. Liu Y., Zhang J, Peng L. M., Three-dimensional integration of plasmonics and nanoelectronics, *Nat Electron*, Vol. 1, 2018, pp. 644-651.

[2]. Mallikarjun G. Hudedmani, Bindu Suresh Pagad, Plasmonics: A. Path to Replace Electronics and Photonics by Scalable Ultra-fast Technology, *Advanced Journal of Graduate Research*, Vol. 7, Issue 1, 2020, pp. 37-44.

[3]. J. R. Sambles, G. W. Bradbery, and F. Z. Yang, Optical excitation of surface plasmons: An introduction, *Contemp. Phys.,* Vol. 32, Issue 3, 1991, pp. 173-183.

[4]. D. K. Gramotnev and S. I. Bozhevolnyi, Plasmonics beyond the diffraction limit, *Nat. Photonics*, Vol. 4, 2010, pp. 83–91.

[5]. W. L. Barnes, A. Dereux, and T. W. Ebbesen, Surface plasmon subwavelength optics, *Nature*, Vol. 424, 2003, pp. 824–830.

[6]. K. Takagi, S. V. Nair, R. Watanabe, K. Seto, T. Kobayashi, E. Tokunaga, Surface plasmon polariton resonance of gold, silver, and copper studied in the kretschmann geometry: dependence on wavelength, angle of incidence, and film thickness, *J. Phys. Soc. Jpn*., Vol. 86, Issue 12, 2017, pp. 1-11.

[7]. Q. Li, Z. Tian, X. Zhang, R. Singh, L. Du, J. Gu, J. Han, W. Zhang, Active graphene–silicon hybrid diode for terahertz waves, *Nat. Commun*., Vol. 6, 2015, pp. 1-6.

[8]. L. Liu, C. Yang, J. Yang, H. Xiang, Dezhuan Han, Spoof surface plasmon polaritons on ultrathin metal strips: from rectangular grooves to split-ring structures, *J. Opt. Soc. Am. B*, Vol. 34, Issue 6, 2017, pp. 1130–1134.

[9]. A. N. Grigorenko, M. Polini, K. S. Novoselov. Graphene plasmonics, *Nat. Photon.,* Vol. 6, 2012, pp. 749–758.

[10]. Tang, P., Zhou, Q., Xu, G., Dirac fermions in an antiferromagnetic semimetal, *Nature Phys.,* Vol. 12, 2016, pp. 1100–1104.

[11]. Z. Wang, H. Weng, Q. Wu, X. Dai and Z. Fang, Three-dimensional Dirac semimetal and quantum transport in Cd_3As_2, *Phys. Rev. B*, Vol. 88, Issue 125427, 2013, pp. 1-6.

[12]. T. Liang, Q. Gibson, M. N. Ali, M. Liu, R. J. Cava, N. P. Ong, Ultrahigh mobility and giant magnetoresistance in the Dirac Semimetal Cd_3As_2, *Nat. Mater*., Vol. 14, 2014, pp. 280–284.

[13]. S. Borisenko, Q. Gibson, D. Evtushinsky, V. Zabolotnyy, B. Büchner, J. R. Cava, Experimental realization of a three-dimensional Dirac semimetal, *Phys. Rev. Lett.,* Vol. 113, Issue 027603, 2014, pp. 1-5.

[14]. Y. Su, Q. Lin, X. Zhai, X. Luo, L. L. Wang, Controlling terahertz surface plasmon polaritons in Dirac Semimetal sheets, *Opt. Mater. Express*, Vol. 8, Issue 4, 2018, pp. 884–892.

[15]. K. J. A. Ooi, Y.S. Ang, Q. Zhai, X. Sun, P. Xing, C. K. Ong, L. K. Ang, D. T. H. Tan, Dirac terahertz plasmonics in two and three dimensions, *Opt. Commun.,* Vol. 462, Issue 125319, 2020, pp. 1-11.

[16]. Zhu, C., Wang, F., Meng, Y. *et al.*, A robust and tunable mid-infrared optical switch enabled by bulk Dirac fermions, *Nat Commun.,* Vol. 8, Issue 14111, 2017, pp. 1-7.

[17]. Xu, H., Guo, C., Zhang, J., Guo, W., Kuo, C.-N., Lue, C. S., Hu, W. D., Wang, L., Chen, G., Politano, A., Chen, X. S., Lu, W., $PtTe_2$-Based Type-II Dirac Semimetal and Its van der Waals Heterostructure for Sensitive Room Temperature Terahertz Photodetection, *Small,* Vol. 15, Issue 1903362, 2019, pp. 1-7.

[18]. Léonard, François *et al*., Strong Photothermoelectric Response and Contact Reactivity of the Dirac Semimetal ZrTe5, *ACS Applied Materials & Interfaces,* Vol. 9, Issue 42, 2017, pp. 37041-37047.

[19]. Duc Anh Nguyen, Dae Young Park, Juchan Lee, Ngoc Thanh Duong, Chulho Park, Duc Hieu Nguyen, Thi Suong Le, Dongseok Suh, Heejun Yang, Mun Seok Jeong, Patterning of type-II Dirac semimetal $PtTe_2$ for optimized interface of tellurene optoelectronic device, *Nano Energy,* Vol. 86, Issue 106049, 2021, pp. 1-10.

[20]. T. M. Blessan and N. Yogesh, Terahertz surface plasmon polariton resonances and microparticle sensing in bulk Dirac semimetal with spatially perturbed geometries, *J. Opt. Soc. Am. B*, Vol. 38, Issue 8, 2021, pp. 2261-2266.

[21]. T. M. Blessan, C. Venkateswaran and N. Yogesh, All- optical terahertz logic gates based on coupled surface plasmon polariton subwavelength waveguiding in bulk Dirac semimetal, *Optik*, Vol. 257, Issue 168795, 2022, pp. 1-9.

[22]. T. Zhao and Z. Wu, Cherenkov terahertz radiation from Dirac Semimetals surface plasmon polaritons excited by an electron beam, *Chinese Phys. B*, Vol. 29, Issue 034101, 2020, pp. 1-10.

[23]. Z. Dai, M. Manjappa, Y. Yang, T. C. W. Tan, B. Qiang, S. Han, L. J. Wong, F. Xiu, W. Liu and R. Singh, High Mobility 3D Dirac Semimetal (Cd_3As_2) for Ultrafast Photoactive Terahertz Photonics, *Adv. Funct. Mater.*, Vol. 31, Issue 2011011, 2021, pp. 1-9.

[24]. http://www.comsol.com

[25]. Hooper, I., Tremain, B., Dockrey, J. *et al*, Massively Sub-wavelength Guiding of Electromagnetic Waves, *Sci Rep.*, Vol. 4, Issue 7495, 2014, pp. 1-5.

[26]. Yuan, Q. Wang, Y. Li, Y. Xu, Q. Xu, X. Zhang, X. Zhang, J. Han, W. Zhang. Terahertz spoof surface plasmonic logic gates, *iScience*, Vol. 23, Issue 101685, 2020, pp. 1-13.

[27]. E. H. Charles, P. R. Buskohl, C. E. Tabor, R. L. Harne, Digital logic gates in soft, conductive mechanical metamaterials, *Nat. Commun.*, Vol. 12, Issue 1633, 2021, pp. 1-8.

[28]. M. V. Sonth, G. Srikanth, P. Agrawal, B. Premalatha. Basic logic gates in two-dimensional photonic crystals for all optical device design, *Int. J. Electron. Telecommun.*, Vol. 67, Issue 2, 2021, pp. 247–261.

[29]. M. Yarahmadi, M. K. Moravvej-Farshi and L. Yousefi, Subwavelength Graphene-Based Plasmonic THz Switches and Logic Gates, *IEEE Transactions on Terahertz Science and Technology*, Vol. 5, Issue 5, 2015, pp. 725-731.

[30]. Xiaomei Yao, Shengxi Zhang, Qiang Sun, Peizong Chen, Xutao Zhang, Libo Zhang, Jian Zhang, Yan Wu, Jin Zou, Pingping Chen, and Lin Wang, Thickness-Controlled Three-Dimensional Dirac Semimetal for Scalable High-Performance Terahertz Optoelectronics, *ACS Photonics*, Vol. 8, Issue 6, 2021, pp. 1689-1697.

Sensors & Transducers, Vol. 258, Issue 4, July 2022, pp. 18-24

Sensors & Transducers

Published by IFSA Publishing, S. L., 2022
http://www.sensorsportal.com

High-speed Wavelength Division Multiplexing Transmission over SI-Polymer Fibers

[1, *] Ulrich H. P. Fischer and [2] Mladen Jóncic

[1] Harz University of Applied Sciences, Friedrichstr. 57, 38855 Wernigerode, Germany
[2] Volkswagen AG, 38518 Gifhorn, Germany
[1] Tel.: +49-(0)3943-659351 fax: +49-(0)3943-659399
E-mail: ufischer@hs-harz.de

Received: 10 June 2022 /Accepted: 17 July 2022 /Published: 29 July 2022

Abstract: In short-range communication 1 mm PMMA SI-POF established itself as a reasonable alternative to the traditional data communication media such as glass fibers, copper cables and wireless systems. Due to multiple advantages such as a large core diameter, tolerance to fiber facet damages and low installation costs, the SI-POF is already applied in industrial automation, automotive industry and in-house/office networks. The commercial systems with SI-POF use a single channel for data transmission. Utilization of several optical carriers for parallel transmission of data channels over a single fiber, known as WDM, represents another alternative to increase the capacity of SI-POF link. To experimentally demonstrate the feasibility and potential of a high-speed POF WDM concept, a four-channel data transmission setup was realized. In addition, the record 14.77 Gb/s data rates employing the offline-processed DMT modulation were demonstrated over 50 m SI-POF, respectively, at the BER=10^{-3}. Compared to the fastest single-wavelength systems, two times higher transmission capacity was achieved

Keywords: Polymeric optical fibers, WDM transmission, WDM Multiplex, WDM Demultiplex, WDM over POF.

1. Introduction

Having its origin in the 1960's as well as the silica glass fiber, the polymer optical fiber (POF) stayed long in the shadow of the huge development and success of glass fiber communications. However, the advances in POF technology and the growing need for high-speed short-range communication networks make POF nowadays gain more and more in importance. The key advantage of POF is a large core diameter. It makes POF tolerant to the fiber facet damages and relaxes the alignment tolerances, thus also reducing the installation costs.

Furthermore, POF is pliable, durable, and inexpensive, offers small weight and short bend radius, allows easy installation, simple termination and quick troubleshooting, and also provides the immunity to electromagnetic interference. Due to its diverse advantages, in short-range applications POF established itself as a reasonable alternative to the traditional data communication media such as glass fibers, copper cables and wireless systems (see Table 1).

Today, POF is produced with different core materials, core diameters and index profiles. Two major POF types are made of polymethyl methacrylate (PMMA) and perfluorinated (PF) materials. The parameters of the common PMMA and PF POFs are specified in the IEC Standard 60793-2-40, which defines eight different POF classes [1].

Table 1. Comparison of different transmission media; Characteristics very bad (--) to very good (++).

Transmission medium	Data rate	Distance	Safety	Cost	Handling	Installation	Total
Twisted pair cable	+	0	0	++	-	0	**2+**
Coaxial cable	0	0	0	+	0	0	**1+**
Glass fiber	++	++	++	--	--	-	**1+**
Polymer fiber	0	-	++	+	+	+	**4+**
Wireless	--	-	--	++	++	++	**1+**
Powerline	-	-	--	+	+	++	**0**

The PMMA POF is produced with both step-index (SI) and graded-index (GI) profile, whereas the PF POF offers only GI profile. The GI profile of the core ensures high modal bandwidth exceeding 1.5 GHz × 100 m for the PMMA POF and 300 MHz × 1 km for the PF POF. However, the implementation of the PMMA GI-POF is confined to 500-680 nm wavelength range due to the high optical attenuation at other wavelengths (> 400 dB/km). The PF GI-POF is best suited for use in the infrared region, e.g. in the first (850 nm) and the second (1300 nm) optical window, where of-the-shelf components developed for multimode glass fibers are available. In contrast, the PMMA SI-POF suffers from intermodal dispersion limiting the bandwidth-length product to around 50 MHz × 100 m (see [2]), but also provides several attenuation windows in the visible spectrum (400-700 nm). Due to its advantages over the other POF types such as technological maturity, ease and cost of production and high numerical aperture (NA), the standard 1 mm PMMA SI-POF (POF class A4a.2 according to IEC 60793-2-40) is the best known and by far the most widely employed type of POF. This is also the fiber the paper concentrates on. Throughout the work the terms SI-POF and POF will be equally used to address this fiber type. A comprehensive overview on various POFs is given in [3].

Three major application sectors of SI-POF data communication technology are industrial automation, automotive industry and in-house/office networks.

The commercial systems with SI-POF use a single channel for data transmission. However, the data carrying capacity of SI-POF is impaired by strong inter-modal dispersion and high optical attenuation. Over the last few years various concepts to overcome the bandwidth limitation of SI-POF have been successfully demonstrated, including optimization of the optoelectronic components and implementation of the digital signal processing techniques. The bus systems such as Profibus (1.5 Mbit/s, 60 m) and industrial Fast Ethernet (100 Mbit/s, 50 m) are typical applications and since 2013 also the Gigabit Ethernet transceivers (1 Gb/s) are available on the market enabling the transmission of broadband services over 50 m SI-POF [4].

1.1. Capacity Extension by WDM Technology

The most frequently mentioned motivation for POF WDM is to increase the transmission capacity of SI-POF link compared to the single-wavelength systems.

Complying with any of the hitherto developments, utilization of several optical carriers for parallel transmission of data channels over a single fiber represents another alternative to increase the transmission capacity of SI-POF. The technique is well known as wavelength division multiplexing (WDM). In glass fiber communications WDM has been firmly established for more than two decades and represents the key technology in modern high-capacity optical networks with the distances ranging from several thousand down to ~100 km [5], [6], [7].

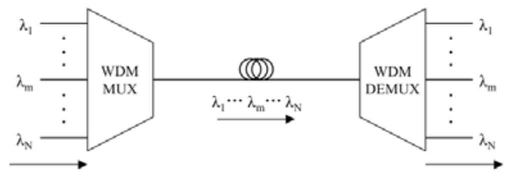

Fig. 1. Principle of WDM: MUX – Multiplexer, DEMUX – Demultiplexer.

The principle of WDM is shown in Fig. 1. Since different wavelengths λ_1–λ_N do not interfere with each other in a linear medium, they can be used to simultaneously carry the data signals over a single fiber. Two components are essential for WDM, a wavelength multiplexer and demultiplexer. The multiplexer combines the signals at different wavelengths, coming from different transmitters, onto a single fiber. On the opposite side of the optical link the demultiplexer performs an inverse function, separating the wavelength channels to be detected by separate receivers. Because of e.g. interchannel crosstalk, the demultiplexer is more often considered in fiber optics. Therefore, this thesis concentrates on the demultiplexing function without loss of generality for the multiplexing operation.

The existing WDM components developed for single-mode glass fibers in the infrared region, such as Mach-Zehnder interferometers, arrayed waveguide gratings or fiber Bragg gratings, cannot be reused for a highly multimode SI-POF. On the other hand, the operating principles of demultiplexers based on thin-film interference filters and on a diffraction grating can be applied for POF. In spite of some other demultiplexing solutions (e.g. employing dispersion prisms), these two demultiplexing techniques have been recognized as the most promising for SI-POF. However, because of the difference in the operating wavelength range, fiber diameter, NA, etc. compared to the glass fibers, such demultiplexers must be newly designed for SI-POF communication. The paper concentrates on the demultiplexing techniques employing thin-film interference filters and a concave diffraction grating.

In the early attempts, the LED-based POF systems exploiting WDM technology could not provide sufficient capacity [8], [9]. Only recently, supported by the advance in the visible laser diode technology, the record-breaking POF WDM transmission experiments, including the work of the author, were performed [10-12].

2. POF Multiplexer

As mentioned on Chapter 1.1, the multiplexer can be realised in a simpler way than the demultiplexer. The principal idea of a small device is shown in Fig. 2. A FC/PC connector was used to combine 4 incoming small POFs with diameters of 400 µm in a plug and couple this plug in a connector to a 980/1000 µm SI-POF. The NA of the incoming 400µm POFs is the same as the SI-POF of 0.5. Since the numerical aperture of both fiber types is identical, the losses in the connection from connector to connector are very low.

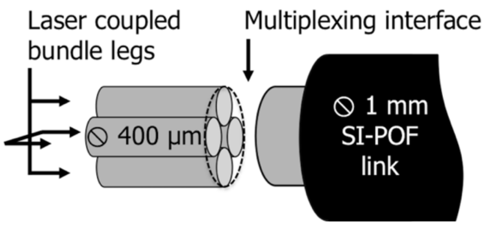

Fig. 2 Principale of operation.

In addition, the fibers are butt-coupled at the end face, so that losses due to reflection at air gaps are avoided. The Performance of the device has measured insertion losses between 3.3 dB – 5.5 dB. The losses are based on launching coupling loss between the two fiber types. Additionally, losses are coming from the attenuation of bundle leg and from the multiplexing interface.

A photograph and the technical setup is shown in Fig. 3. A FC/PC connector combines the two FC/PC plugs with the different fiber types and a simple setup of the optical multiplexer for POF was realised.

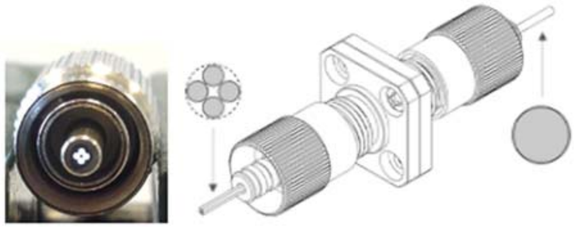

Fig. 3. Practical realisation in a FC/PC connector.

3. For Channel Demultiplexer

The demultiplexer was realized with the components from LINOS Microbench series and was installed on a vibration suppressing optical table. The principle of operation of a four-channel demultiplexer with two-stage configuration is shown in shown in Fig. 4. A 4-rod construction system supported with the mounting holders was used to bring together the Microbench mechanical components holding the fibers and bulk optical elements. The ingoing and the outgoing fibers, which were terminated with SMA connectors, were mounted over SMA fiber adapters into XYZ fine adjustment units. The units provided a travel range of ±1 mm in the x- and y-direction, and when anchored to the 4-rod system allowed a travel of 5 mm along the optical axis (z-direction). The aspheric lenses were mounted in XY precision translation stages having a travel range of ±1 mm along the x- and y-direction. The collimating lens with 25 mm mounting diameter was directly mounted in the stage, whereas the focusing lenses with a smaller mounting diameter were mounted over reduction inserts. In each of the output ports the bandpass interference filter was mounted in the XY precision translation stage in front of the aspheric lens. The dichroic mirrors are glued to an adjustable mirror insert was positioned within a beam splitter cube over a rotation adjustment for cube insert.

In Fig. 5 a photograph of the mechanical and optical setup is depicted. The first stage of the demultiplexer, represented by a dichroic mirror that follows directly after the collimating lens, split the incident spectrum into two spectral bands. The separation of the individual wavelength channels was then performed within the second stage of the demultiplexer.

Accordingly, the demultiplexer setup allowed very precise positioning and alignment of the fiber end faces, lenses and dichroic mirrors. The available degrees of freedom can be summarized as follows:

- End faces of the ingoing and the outgoing fibers: x-, y- and z-direction translation;
- Collimating and focusing lenses: x- and y-direction translation;

- Dichroic mirrors: rotation and tip/tilt (when applied together tip and tilt result in translation along the direction perpendicular to the incoming optical axis).

To measure the transfer function of the demultiplexer, a Yokogawa AQ4305 white light source followed by a cylinder mode mixer according to JIS 6863 provided a wide spectral range (400-700 nm) to the input of the demultiplexer. The spectral responses of the channels were recorded by a Yokogawa AQ-6315A optical spectrum analyser.

Table 2. Basic parameters of four channel multiplexer.

Output port	1	2	3	4
Center wavelength [nm]	404.9	450.1	528.3	646.4
3 dB passband bandwidth [nm]	9.4	9.3	41.6	47.6
Minimum IL [dB]	5.66	4.55	3.47	3.19
IL uniformity [dB]	2.47			
(Non)adjacent channel isolation [dB]	> 30			

The corresponding transfer function is shown in Fig. 6. The basic parameters of the demultiplexer are given in Table 2. The measurement results for the four-channel demultiplexer with two-stage configuration were presented at the International Conference on Plastic Optical Fibers (ICPOF) 2013 [13]. To comply with all other measurements shown in this chapter, which were performed two years thereafter, the demultiplexer setup was assembled and characterized again. While preserving the same principal behaviour of the spectral response, the minimum IL in the output ports 1 to 4 was 6.15 dB, 5.44 dB, 4.21 dB and 3.85 dB respectively. Those were by 0.49 dB, 0.89 dB, 0.74 dB and 0.66 dB higher values than those reported in [14].

The device is well suited for implementation in high-speed POF WDM transmission experiments.

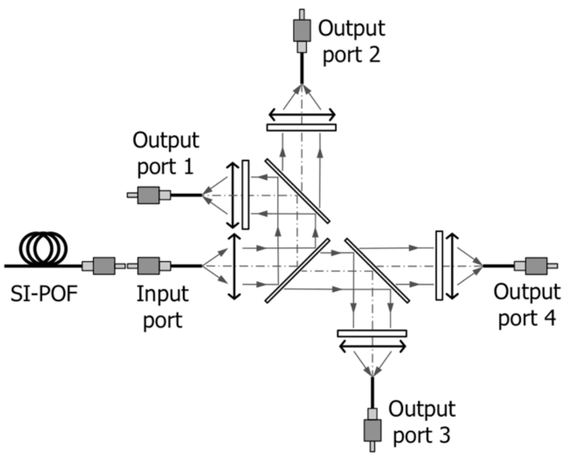

Fig. 4. Principle setup of a four-Channel Demultiplexer with Interference Filters.

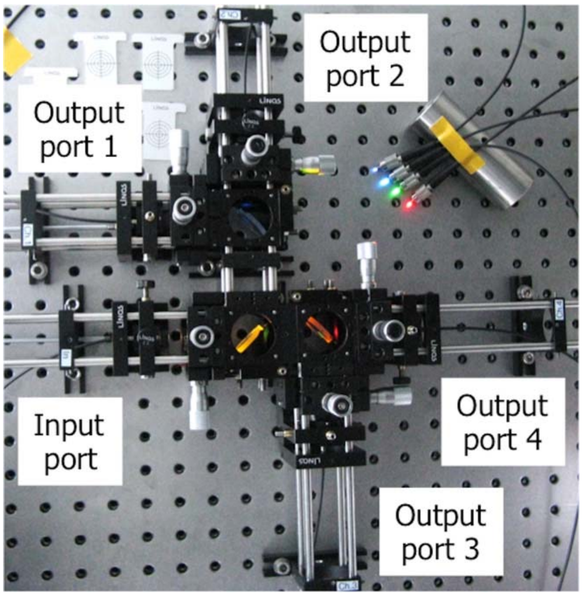

Fig. 5. Realisation of the 4 Channel Demultiplexer.

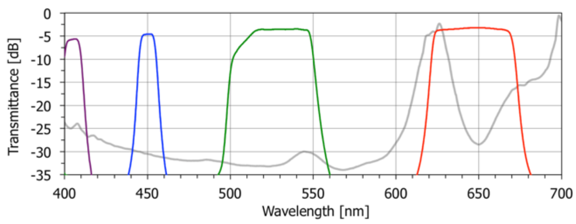

Fig. 6. Transmittance of the Demultiplexer.

4. Four-channel POF WDM Transmission Experiments

The data transmission setup is shown in Fig. 7. It comprised an Agilent N4903A bit error rate tester (BERT), four butt-coupled edge-emitting laser diodes, multiplexing POF coupler, 50/100 m SI-POF link, interference-based POF demultiplexer, optical receivers and Agilent 86100B sampling oscilloscope.

To combine the optical signals (MUX) with different wavelengths onto the SI-POF link, a Comcore 4×1 fused POF coupler was used. For direct launching with 405 nm (DL-5146-101S), 450 nm, 515 nm and 639 nm laser diodes, the IL between any of four input (laser coupled) ports and the output port was 8-9 dB.

The experimental setup for the measurements employing the offline-processed DMT modulation is shown in Fig. 7. It comprised the four-channel Agilent M8190A AWG, four butt-coupled edge-emitting laser diodes, four-legged multiplexing POF bundle, SI-POF link of two different lengths (50, 100m), interference-based POF demultiplexer, optical receivers, four-channel Agilent DSA91604A real-time oscilloscope and computer with a software for offline signal processing.

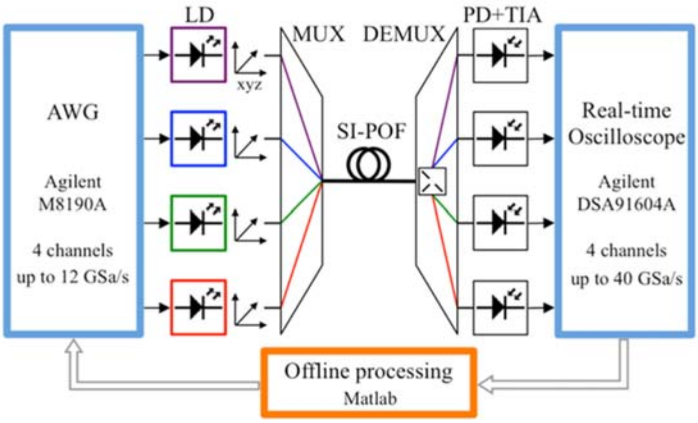

Fig. 7. Experimental setup for the measurements employing offline-processes DMT modulation: LD – laser diode; MUX – multiplexer; DEMUX – demultiplexer; PD – photodiode; TIA – transimpedance amplifier.

The photograph of the electrical and optical setup can be seen in in Fig. 8. Here the following components are depicted:

1- DMT AWG;
2- RF amplifier for LD modulation;
3- RF – Y-Connectors for the LDs;
4- LD Cooler;
5- LD Cooler controller slot;
6- LD Cooler input device hub Tektronix;
7- Multiplexer;
8- 50m Si-POF;
9- Demultiplexer;
10- High speed optical Receiver;
11- Real time Oscilloscope;
12- Optical integration sphere;
13- Optical power meter.

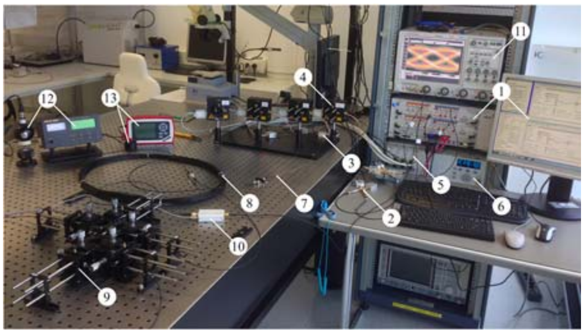

Fig. 8. Experimental Data transmission setup.

4.1. Experimental Results

To estimate the quality of the WDM channels and allocate the number of bits per subcarrier, four DMT pilot signals with 256 subcarriers, each loaded with 16-QAM, were simultaneously transmitted over four channels. In 50 m and 100 m experiments the bandwidth occupied by the pilot signals was initially set to 1 GHz and 500 MHz respectively.

To decorrelate the signals that modulated the laser diodes, an additional delay of 10 ns between the channels was introduced in the AWG. The received signals were demodulated and used to evaluate the SNR per subchannel. For the case the SNR in the highest subchannels was high enough to allow transmission of additional bits at even higher subcarrier frequencies, the bandwidth of the pilot signal was accordingly increased and the measurement was repeated.

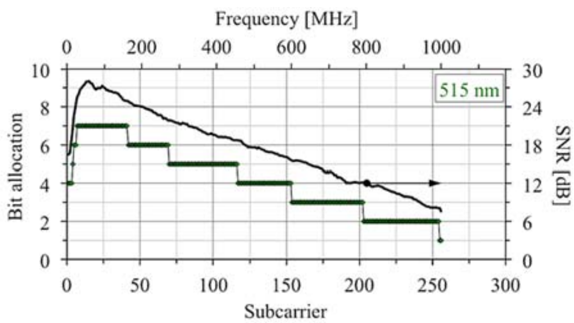

Fig. 9. Measured example SNR per subcarrier before bit-loading (solid black curve) and bit-loading scheme obtained on the basis of Chow's rate adaptive bit-loading algorithm (curve with markers) for the 515 nm channel in 50 m POF experiment.

The evaluated SNR per subchannel was used as input to the Chow's rate adaptive bit-loading algorithm that computed the appropriate bit-loading scheme and power allocation per subchannel [15]. Based on the obtained bit and power allocations across the subcarriers, the real-valued samples of the DMT time signal were pre-computed offline. After that, the DMT samples were loaded into the memory of the AWG and repeatedly played in order to create a continuous-time DMT signal that directly modulated the intensity of the laser diode. The received DMT frames were captured by the oscilloscope for subsequent offline processing that comprised DMT demodulation, SNR evaluation and BER counting.

After deduction of the DMT transmission overhead, the data rates transmitted in the individual WDM channels were 3.26 Gb/s (405 nm channel), 3.90 Gb/s (450 nm channel), 4.08 Gb/s (515 nm channel) and 3.53 Gb/s (639 nm channel). The total averaged BER in each channel was 10^{-3} allowing the FEC with 7 % overhead. Therefore, an aggregate bit rate of 14.77 Gb/s achieved at the BER=10^{-3} corresponded to 13.8 Gb/s information bits at the BER<10^{-9}. A measured example of the bandwidth of the subcarrier behavior of the green Channel at 515nm is depicted in Fig. 9.

In Fig. 10 the measured symbol bits are depicted. The measurement represents a superimposed constellation diagram of the subcarrier group modulated with 4-QAM (182nd to 185th and 191st to 232nd subcarrier). An averaged received SNR for the subcarrier groups modulated with 256-QAM and 4-QAM, obtained from the measurement data from Fig. 5.16a, equals 29.22 dB and 9.76 dB respectively.

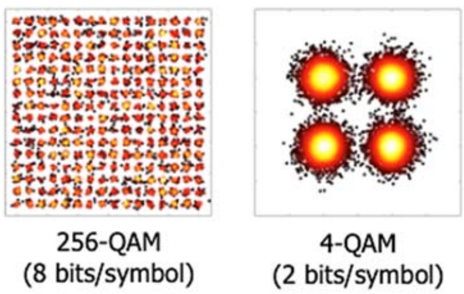

Fig. 10. Measured QAM signals with 256/8bits/symbol (left) and 4 QAM with 2bit/symbol (right).

Table 3. Comprehension of measured data rates for 4 channels via 50m and 100m SI-POF.

WDM channel	50 m	100 m
Violet 405 nm	3.26 Gb/s	1.34 Gb/s
Blue 450 nm	3.90 Gb/s	2.09 Gb/s
Green 520 nm	4.08 Gb/s	2.84 Gb/s
Red 656 nm	3.53 Gb/s	1.99 Gb/s
Total (BER=10^{-3})	**14.77 Gb/s**	**8.26 Gb/s**
Error free (with FEC)	**13.80 Gb/s**	**7.72 Gb/s**

Therefore, an aggregate bit rate of 14.77 Gb/s achieved at the BER=10^{-3} corresponded to 13.8 Gb/s information bits at the BER<10^{-9}. All data rates measured for the four transmission channels via 50m and 100m SI POF are listed in Table 3. The realized system provided 2.3 times more capacity than the fastest 50 m single-wavelength system known from literature, which operated at 650 nm [16].

5. Conclusions

In this work it was shown, that WDM transmission over POF realised a huge extension of overall data rates within one fiber over 50 m. The 14.77 Gb/s data transmission based on the offline-processed DMT modulation was demonstrated over 50 m SI-POF at the BER=10^{-3}. That is the second highest transmission capacity ever achieved over 50 m SI-POF.

Enabling higher WDM data rates, it will be possible to reach data rates for POF WDM Systems with up to 40 Gbit/s with 16 WDM channels.

Acknowledgements

We thank the German Federal Ministry of Research (BMBF) for support this work under project HOPE (**H**igh speed **O**ptical transmission over **P**olym**E**r fibers)

References

[1]. T. Specification, IEC09, and T. Specification, TS 105 175-1 - V1.1.1 - Access, Terminals, Transmission and Multiplexing (ATTM); Plastic Optical Fibre System Specifications for 100 Mbit/s and 1 Gbit/s, Vol. 1, pp. 1–16, 2010.

[2]. J. Zubia and J. Arrue, Plastic Optical Fibers: An Introduction to Their Technological Processes and Applications, *Opt. Fiber Technol.*, Vol. 7, No. 2, 2001, pp. 101–140.

[3]. O. Ziemann, J. Krauser, P. E. Zamzow, POF Handbook: Optical Short Range Transmission Systems., *Springer Verlag*, Berlin Heidelberg, 2008.

[4]. K. L. Johnson, W. Hogan, M. M. Dummer, and C. Steidl, Advances in High-Speed Red Vcsel Performance, *Adv. Opt. Technol.*, Vol. 2012, 2012, pp. 5–10.

[5]. B. Mukherjee, WDM optical communication networks: progress and challenges, *Sel. Areas Commun. IEEE J.*, Vol. 18, No. 10, 2000, pp. 1810–1824.

[6]. S. V. Kartalopoulos, DWDM: Networks, Devices, and Technology, *Wiley-IEEE Press*, 2002.

[7]. H.-J. Thiele and M. Nebeling, Coarse wavelength division multiplexing: technologies and applications, *CRC Press*, 2007.

[8]. P. J. Pinzón, I. Pérez, and C. Vázquez, Visible WDM System for Real-Time Multi-Gb/s Bidirectional Transmission over 50-m SI-POF, *IEEE Photonics Technol. Lett.*, Vol. 28, No. 15, 2016, pp. 1696 – 1699.

[9]. X. Li *et al.*, 11 Gb/s WDM transmission over SI-POF using violet, blue and green μlEDs, in *Proceedings of the Optical Fiber Communications Conference and Exhibition (OFC 2016)*, 2016, paper Tu2C.5.

[10]. R. Kruglov, J. Vinogradov, S. Loquai, O. Ziemann, C.-A. Bunge, T. Hager, 21.4 Gb/s discrete multitone transmission over 50-m SI-POF employing 6-channel WDM, in in *Proceedings of the OFC/NFOEC*, 2014, paper Th2A.2.

[11]. M. Joncic *et al.*, Four-Channel WDM Transmission Over 50-m SI-POF at 14.77 Gb/s Using DMT Modulation, *Photonics Technol. Lett. IEEE2*, Vol. 26, No. 13, 2014, pp. 1328–1331.

[12]. I. Yahav, N. Sheffi, Y. Biofcic, and D. Sadot, Multi-Gigabit Spatial-Division Multiplexing Transmission over Multicore Plastic Optical Fiber, *J. Light. Technol.*, Vol. 39, No. 8, Apr. 2021, pp. 2296–2304.

[13]. U. F.-H. [Joncic13c] M. Jončić, M. Haupt, Development status of a four-channel CWDM system for Multi-Gbit/s in-house data communication via SI-POF, *20. ITG-Fachtagung Kommun.*, p. 6, 2013.

[14]. U. H. P. P. Fischer, S. Höll, M. Haupt, and M. Joncic, Integrated Optical Demultiplexer for WDM Communication Systems, in *Proceedings of the 6th Electronics System-Integration Technology Conference*, 2016, p. 155.

[15]. P. S. Chow, J. M. Cioffi, and J. A. C. Bingham, A practical discrete multitone transceiver loading algorithm for data transmission over spectrally shaped channels, *IEEE Trans. Commun.*, Vol. 43, No. 2, 1995, pp. 773–775.

[16]. J. Vinogradov, R. Kruglov, S. Loquai, O. Ziemann, Multi gigabit transmission with blue, green and red laser diodes, in *Proceedings of the 20th International Conference on Plastic Optical Fibers*, 2011, pp. 467–470.

Sensors & Transducers, Vol. 258, Issue 4, July 2022, pp. 25-30

www.sensorsportal.com

Sensors & Transducers

Published by IFSA Publishing, S. L., 2022
http://www.sensorsportal.com

Preflight Preparations for Active Debris Removal and Ranging

[1 *] Claude PHIPPS and [2] Christophe BONNAL
[1] Photonic Associates, LLC, 200A Ojo de la Vaca, Santa Fe, NM 87508, USA
[2] CNES, 52 rue Jacques Hilairet, 75612 Paris Cedex, France
[1] Tel.: +1-215-358-4360, fax: +1-505-466-3877
E-mail: crphipps@aol.com

Received: 8 June 2022 /Accepted: 15 July 2022 /Published:29 July 2022

Abstract: In this paper we present three technical improvements that will better prepare satellites for their later removal prior to launch, in accordance with international agreements such as the IADC Space Debris Mitigation Guidelines, which ensure that satellites are designed to re-enter within 25 years. Space debris are non-functional satellites orbiting the Earth, such as abandoned second stage rockets, nanosatellites (most of which have no onboard propulsion) and collision fragments including those from deliberate destruction. Just-in-time Collision Avoidance (JCA) can prevent anticipated collisions. It requires far more precise orbit parameters for debris than we have now. The main tool we will use is ultra-precise laser ranging from an orbiting ranging station, which can operate up to 500 km range from a debris, provided it has good optical cross-sections. To enhance cross-sections, we would install 1-cm optical corner reflectors on each satellite, four around its equator and two at its poles so that one or more will always be visible. We compare pulsed and frequency-chirped CW lasers in this regard. To better optimize energetic efficiency of laser propulsion to nudge satellites away from a predicted collision, we suggest the Thomson scattering technique, which permits simultaneously measuring the change of target velocity and the plume exhaust velocity, which can be combined to calculate this efficiency in real time.

Keywords: Laser ranging, Just in time collision avoidance, Picosecond laser, Thomson scattering, Chirped-frequency CW laser.

1. Introduction

We have discussed laser Active Debris Removal (ADR) extensively, including precise ranging[1,2] sufficient to reduce false collision alarms from 100/year to 0.02/year. In those works, we assumed the laser pulse originating from a spaceborne laser station scatters off a target satellite into PI steradians. At 1000 km range, the ranging system needed a 50 mJ, 100 ps pulsed laser and 75cm diameter optical aperture to attain adequate signal to noise (S/N) ratio. In this paper, we discuss prelaunch satellite modifications that can permit low power CW lasers to be used for ranging. A second (high power) pulsed laser is needed for the ultimate ”laser nudging” operation to prevent subsequent predicted collisions.

We propose three simple improvements in procedure to better prepare satellites for ADR at end of life if they become derelicts unable to re-enter themselves. These are enhancing satellite laser signal cross section and attaching special thrust plates to improve thrust direction control in “nudging,”[2] prior to launch, and implementing measurement of shot-to-shot kinetic efficiency during nudging. We also discuss ways to optimize ablation kinetic efficiency and to select optimum ablation fuels that could withstand millions rather than thousands of shots.

2. Pre-launch Preparation

2.1. Corner Reflectors

We can enhance laser signal cross section for easier Just-in-Time Collision Avoidance activities (JCA) by installing as few as six small corner reflectors (not refractive corner cubes) on the satellite surface.

A single 1-cm open corner reflector (Fig. 1) provides 4.4×10^{11} increase in brightness of the ranging laser return, compared to a simple rough metal surface scattering into PI steradians. Four around the satellite equator and two at the poles will suffice because a corner reflector has a 90-degree field of view (FOV) [4].

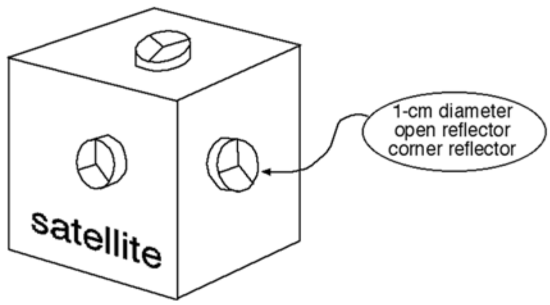

Fig. 1. Small corner reflectors on a satellite.

Corner cubes have smaller FOV. To achieve even greater brightness, a 10-cm patch of corner reflectors could be installed if it will not interfere with satellite operation (Fig. 2).

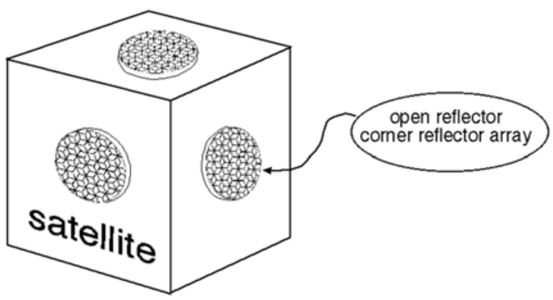

Fig. 2. Larger reflector patches on satellite.

Patches you see on highway signs are deliberately broadened and less bright, but we've all seen how effective they are. The post-Newtonian corrections due to Gambi [5, 6] must still be observed when pointing the laser beam. However, satellite rotation is not one of these. A target satellite rotating at 10 degrees/s at 500km would only cause a few µm repositioning error of the return beam on the laser station because photons spend only a few tens of ps inside the reflector elements, and beam pointing error due to satellite rotation is about 6 picoradians.

2.2. Thrust Plate to Control Nudging Laser Thrust Vector

Normally, thrust is perpendicular to the satellite surface, independent of the laser beam incidence angle. Fig. 3 shows a conceptual thrust plate composed of an array of ablative fuel hemispheres which can produce a thrust vector counter to the laser beam instead.

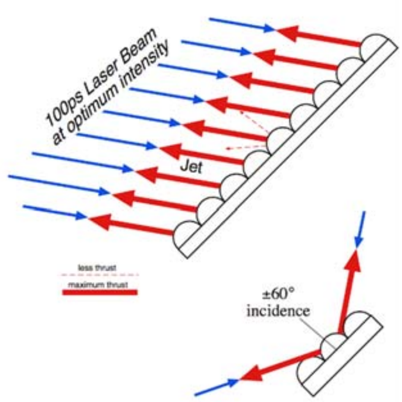

Fig. 3. Special Thrust Plate.

Note that we have not actually built and tested this device, but it will work as advertised if the laser intensity is tightly controlled to match the optimum ablation intensity at the surface normal of the thrust plate hemispheres. This device will have a 120° range of laser incidence angles using 100 ps pulses. This will allow us to better control target motion after impact of a high energy single laser pulse.

Nudging is done with a 0.1-1 kJ pulsed laser system similar to that in [3].

To be complete, we remind the reader that, with very high laser intensities, where plasma velocity v_p is relativistic, thrust can be tilted relative to surface normal without special arrangements (Fig. 4).

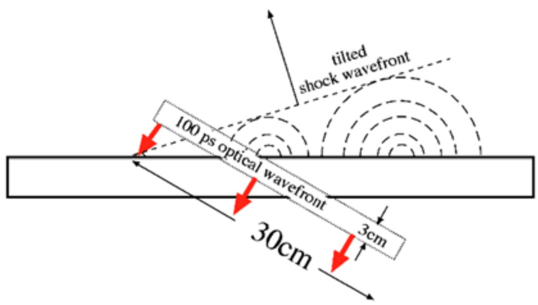

Fig. 4. Thrust vector with very hot plasmas can tilt relative to surface normal (angles exaggerated).

3. Chirped CW Laser

There is significant interest in using low power CW lasers (rather than 100 ps pulses) to locate debris in the JCA program. In this section, we will show that just 250 mW CW in a suitably "chirped" 1064 nm beam will provide adequate S/N at a range up to 500 km while locating targets within 1.5 cm.

Fig. 5 illustrates our laser pulse format. For this idea, we are indebted to a very well written thesis [7].

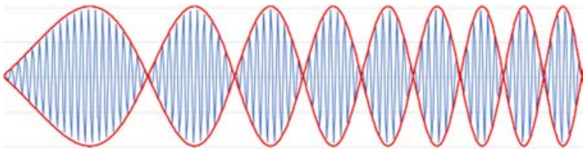

Fig. 5. Amplitude-modulated optical wave with chirped modulation frequency.

The Fig. 5 waveform is described by Eq. (1) with

$$E = \sin(\omega_1 t)\sin(\omega_2(1+bt)t) \quad (1)$$

ω_1 the optical wave, and $\omega_2(1+bt)$ the linearly chirped amplitude modulation. We cannot perform direct operations on the optical wave without a complex optical interferometer. However, we can cross-correlate the returning (time-reversed) AM modulation pattern (shown in red) with a copy of that for the outgoing wave and select the peak to determine range.

Table 1 shows the numerical results for this system.

Table 1. Numerical results for CW laser ranging.

Wavelength	1064	nm
Mirror diameter	75	cm
M^2	1.5	
Max Target Range	500	km
Beam dia. on target	1.91	m
Search area dia. (solar illum	100	m
Laser pulse duration	10	ms
Laser power	250	mW
Chirp bandwidth	5	GHz
Corner reflector diameter	1	cm
Signal brightness at rcvr.	2.61	W/(m^2sr-um
Background brightness	2.70E-06	W/(m^2sr-um
S/N	9.70E+05	
Photodetector efficiency	70	%
S/dark current	6300	
Target location precision	1.5	cm
Precision interval (p.i.)	33	ps
Photoelectrons in p.i.	1310	
Quarter optical period T/4	50	ps
Phtoelectrons in T/4	1960	
Beat freq. at 500km	1.67	GHz

The optical frequency ω_1 is 282 THz. If we select b=500 GHz/s, the chirped modulation frequency covers a 5 GHz band and the spacial resolution c/(4B) =1.5 cm [8]. Chirped laser pulse duration is 10 ms at 250 mW at 1064 nm, giving a 2.5 mJ transmitted pulse energy. This precision is similar to our results with the 50 mJ, 100 ps pulsed laser source we discussed in [1] for ordinary satellite surfaces without corner reflectors.

Because of the frequency ramp, the return signal will exhibit a beat frequency when mixed with the outgoing signal (Fig. 6). For a stationary target, this freqency, f_B contains the range z. For range 500 km, the round trip delay 2 z/c is 3.33 ms, and the beat frequency will be 1.67 GHz.

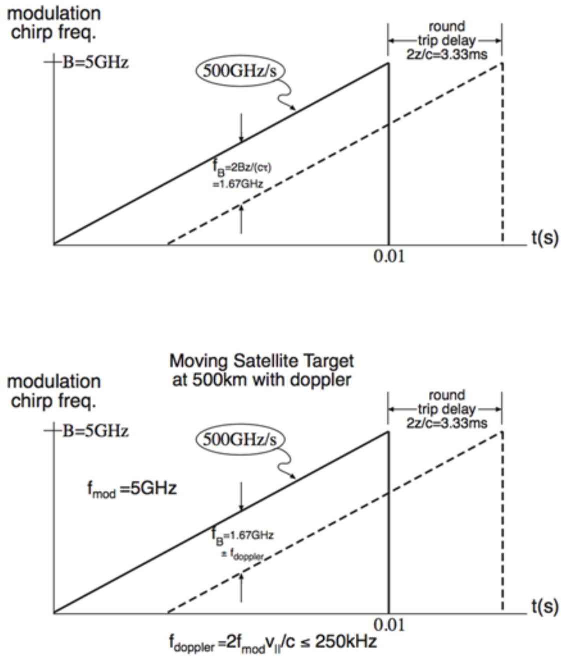

Fig. 6. Return signal with a) stationary and b) moving targets. The chirped pulse repeats every 10 ms.

However, if we consider a moving target with a 7.5 km/s velocity component parallel to the laser beam, f_B now contains an additional 250 kHz doppler component (Fig. 6b). To deal with this, three actions will be sufficient:

(1) Add one more modulation to the outgoing signal, consisting of many sharp (100 ps rise and fall), pseudo-randomly spaced dropouts;

(2) Because the target will have moved 75 m during the 10ms outgoing pulse, gradually stretching the return by 0.25 μs and ruining the possible precision, an onboard computer must recurrently estimate the Doppler frequency and add or subtract an onboard variable frequency oscillator signal from the recorded return until the best precision is obtained. We note that if this step is done perfectly, step 1) may not be necessary, but

we sugest to implement it because of the inevitable effects of noise;
(3) Cross-correlate the modified return with the stored transmitted signal.

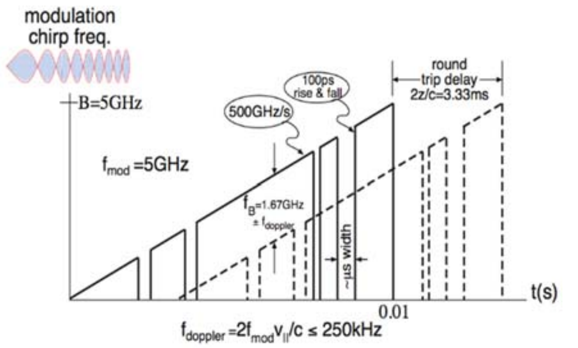

Fig. 7. Pseudo-random code modulation of outgoing signal.

Given these actions, we will obtain a single 100 ps pulse representing the target location with ±1.5 cm precision (Fig. 8).

4. Ranging Procedure

Fig. 9 shows the laser transmit/receive path. The ranging procedure is identical to that in [3], with the difference that the ranging signal is a 250 mW CW 1064 nm, 10 ms laser pulse. First, we find the target with a broad area search, using solar illumination of the target plane (yellow beam in Fig. 9).

Then, we aim the laser at the target and track it, obtaining its range in a few seconds. The telescope is designed to fit inside a Vega-C for launch.

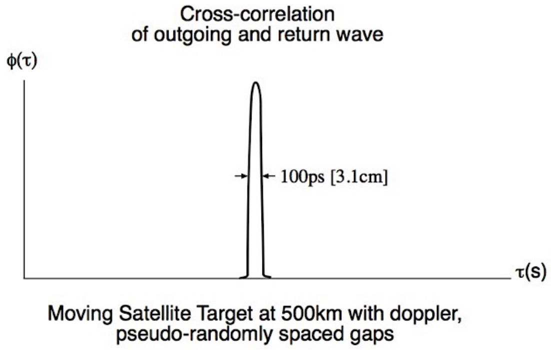

Fig. 8. Result of cross-correlating the outgoing and return signal with Doppler removed.

5. Laser

The laser follows closely the design of Li et al. [8], who achieved 400 Hz bandwidth in their single-frequency oscillator. See [8] for many additional details that are overlooked in the simplified block diagram in Fig. 10. In the Figure, a non-planar ring oscillator (NPRO) feeds an electro-optic modulator (EOM) which is input to a yttrium-doped fiber amplifier (YDFA) that produces 30W. The EOM is driven by a chirp signal generator with a DC bias control system.

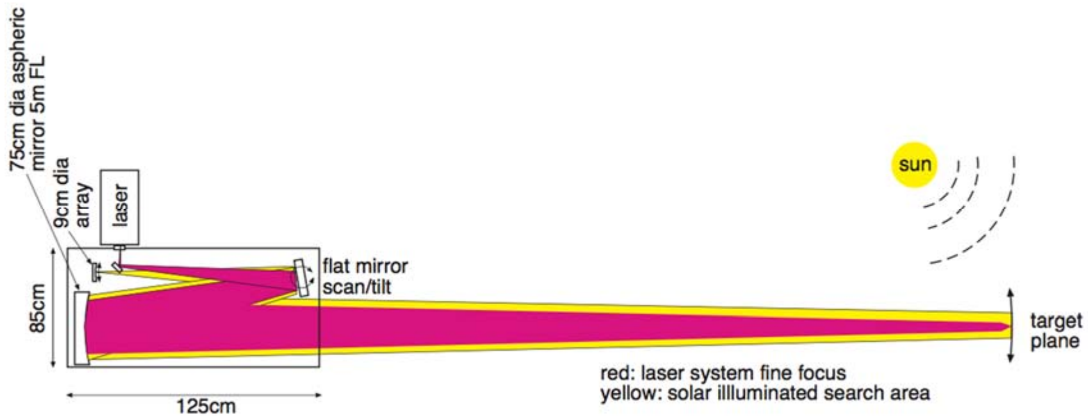

Fig. 9. Laser transmit/receive path to target, and array detector. Range is up to 500 km.

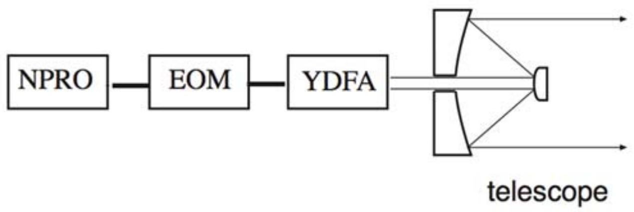

Fig. 10. Laser system block diagram.

6. Optimizing Kinetic Ablation Efficiency in Real Time using Thomson Scattering

Ablation efficiency is given by

$$\eta_{AB} = \Delta m v_i^2 / 2W = C_m v_i / 2 \qquad (1)$$

with laser pulse energy W, momentum coupling coefficient C_m, ablated mass Δm and ion velocity v_i. We determine Cm from Δv_{target} in a single shot, as measured by the system described in §3. The novel approach we describe in this section is to measure ion velocity v_i using the Thomson scattering technique [9, 10], Fig. 11.

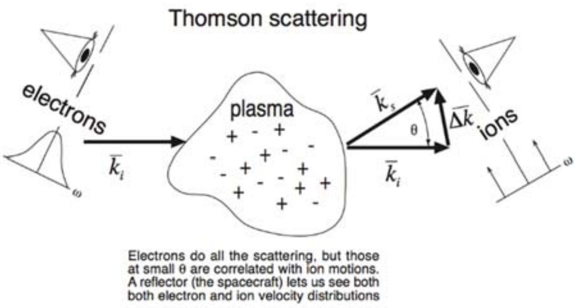

Fig. 11. Thomson scattering principle.

A short pulse laser provides wave vector $\mathbf{k_i}$. In Thomson scattering, the forward (collective scattering) direction gives the ion distribution. Where Δk is the scalar wave vector change and D_e is the electron Debye length, the Thomson scattering shape function in the limit $\alpha = 1/(\Delta k D_e) >> 1$ is

$$S(\Delta k, \omega) = Z \left| 1 + \frac{2T_e}{T_i} W(v/v_i) \right|^2 \frac{e^{-(v/v_i)^2}}{\sqrt{\pi} v_i}. \qquad (2)$$

for a maxwellian plasma, but the technique will give the actual velocity distribution if the plasma is non-maxwellian. In Eq. (2), Z is ion charge state and W is an integral described in [9]. In the backward direction, the electron velocity distribution is given, but we want the ion distribution here. Fortunately, the satellite itself reflects the ion feature back to us. Now, the parameters in Eq. (1) are available to us and we can dither pulse energy W until η_{AB} is maximum. The ion feature is easily distinguished from the electron feature because it is very close to the laser frequency.

7. How to Avoid Melting Propelled Targets

This section, and the one following, refer to an entirely different scenario in which intense, repetitive short pulses (of order 100 ps) are used to propel a space object. Ref. [11] showed that the maximum pulse number to avoid melting can be written

$$N_{max} = (2/3)^{1/3} C_p M (T_m - Ti) / (C_{th} W) \qquad (3)$$

With M indicating target mass, T_m and T_i the melting and initial temperatures, C_{th} the thermal coupling coefficient and W the laser pulse energy. This relationship assumes we heat the entire ablation fuel block, and limits us to about 2,000 pulses for a few-kg aluminum target. In [11], it was stated that a few-kg aluminum debris could not be re-entered without a cooldown. Further, many flights that have been proposed need hundreds of thousands of pulses [13]. There is a solution to this problem: at very high laser intensity on target, surface recession will outrun the thermal wave. If we apply high intensity plasma theory[12], we can achieve conditions in which $v_{rec}/v_{th} >> 1$, as shown in Eq.(4):

$$v_{rec} / v_{th} = 1.26E-6 \frac{A^{7/8}}{\tau^{0.75}[Z^2(Z+1)]^{3/8}} \sqrt{\frac{\Phi}{\lambda \rho}} \qquad (4)$$

In Eq. (4), Φ is fluence (J/m^2), A is average atomic mass number in the plume, Z is average ionic charge, λ is wavelength, K is thermal conductivity of the solid fuel ρ is the solid fuel density (kg/m^3) and τ is laser pulse duration. With typical values for laser space flights (355 nm, 100 ps, 40 kJ/m^2), and properties of calcium silicate, Eq.(4) gives $v_{rec}/v_{th} = 3.2 \times 10^6$.

8. A Figure of Merit for Ablation Fuels

We suggest a figure of merit for long laser ablation flights as shown in Eq. (5):

$$FOM = \frac{\eta_{AB} T_m}{C_{th} K} \qquad (5)$$

This figure of merit emphasizes ablation efficiency and melting temperature, and de-emphasizes thermal coupling coefficient C_{th} and thermal conductivity. Ablation efficiency and C_{th} have not been measured for all materials, but estimates give the results in Table 2, which shows how important refractory materials (rather than low melting metals) will be for ablation fuels in future laser propelled flights.

Table 2. Figure of merit for several ablation fuels.

Matl	EtaAB	Tm	K	Cth	FOM
Fiberglas	0.2	1120	0.04	0.3	1.87E+04
Ca2SiO4	0.2	2130	0.2	0.3	7.10E+03
ZrO2	0.2	2715	1.7	0.3	1.06E+03
CaCO3	0.2	2072	2.25	0.3	6.14E+02
Zr	0.6	3371	16.7	0.3	404
POM	0.2	175	0.31	0.3	376
SiC	0.2	3545	39	0.3	61
Al	0.22	660	239	0.03	20
WC	0.2	2870	110	0.3	17
Graphite	0.06	3600	470	0.15	3.1
	Estimates for materials not measured				

A brief presentation of this work was given as an oral paper in [14].

9. Conclusions

In this paper, we have outlined two preflight actions which will improve laser ranging, a procedure which will permit using a 250 mW CW laser for ranging, and a method to optimize kinetic efficiency in the nudging operation. We also discussed a way to partially control thrust direction and a way to search for better ablation fuels which can take many more than 2,000 pulses before melting.

Acknowledgments

We gladly acknowledge Prof. Sergey Yurish for providing a path to publication for this work, and for his effort in setting up OPAL' 2022.

References

[1]. C. Bonnal, D. McKnight, C. Phipps, C. Dupont, S. Missonier, L. Lequette, M. Merle and S. Rommelaere, Just in time collision avoidance – a review, *Acta Astronautica*, 170, 2020, pp. 637-651.

[2]. C. Phipps and C. Bonnal, A spaceborne, pulsed UV laser system for re-entering or nudging LEO debris, and re-orbiting GEO debris, *Acta Astronautica*, 118, 2016, pp. 224-236.

[3]. C. Phipps, L'ADROIT – A spaceborne ultraviolet laser system for space debris clearing, *Acta Astronautica*, 104, 2014, pp. 243-255.

[4]. S. Somerstein, J. Fuller and R. Kennedy, Retroreflector field of view properties for open and solid cube corners, *SPIE Proceedings*, 1168, 1989.

[5]. J.-M. Gambi, C. Phipps, M. L. Del Pino, M. C. Rodriguez-Teijeiro and J. I. Arana, Post-Newtonian Corrections to JCA, Paper 6.2, in Proceedings of the *6th Workshop on Space Debris Modeling and Remediation*, Politecnico Milano, Italy 18-20 May, 2022.

[6]. J. M. Gambi and M. L. Garcia del Pino, Post-Newtonian tracking formulae to increase the shooting accuracy of autonomous LEO laser trackers, *Adv. in Space Research*, 67, 2021, pp. 2282-2303.

[7]. P. Adany, Simplified homodyne detector for FM chirped lidar, B. S. Thesis, *University of Kansas*, 2007.

[8]. S. Li, S. Yang, Z. Wang and Z. Li, High-power broadband-chirped intensity-modulated single-frequency 1064 nm laser, *Appl. Sci.*, 10, 2020, 4450.

[9]. C. Phipps and D. Bershader, Measurement of nonisotropic electron velocitiy distributions by laser scattering, in Dynamics of Ionized Gases, M. J. Lighthill, I. Imai and H. Sato (Eds.), *University of Tokyo Press*, 1973.

[10]. M. Kaloyan, S. Ghazaryan,C. Constatantin, R. Post, P. Heuer, J. Pilgram, D. Schaeffer and C. Nieman, Raster Thomson scattering in large-scale laser plasmas produced at high repetition rate, *Rev. Sci. Inst.*, 92, 2021, 093102.

[11]. S. Scharring, R. Lorbeer and H.-A. Eckel, Heat accumulation in laser-based removal of space debris, *J. AIAA*, 56, 2018, pp. 2506-2508.

[12]. C. Phipps, T. Turner, R. Harrison, G. York, W. Osborne, G. Anderson, X. Corlis, L. Haynes, H. Steele, K. Spicochi and T. King, Impulse Coupling to Targets in Vacuum by KrF, HF and CO_2 Lasers, *J. Appl. Phys.*, 64, 1988, pp. 1083-1096.

[13]. C. Phipps, C. Bonnal, F. Masson, M. Boustie, L. Berethe, M. Schneider, S. Baton, E. Brambrink, J.-M, Chevalier, L. Videau and S. A. E. Boyer, Transfers from Earth to LEO and LEO to interplanetary space using lasers, *Acta Astronautica*, 146, 2018, pp. 92-102.

[14]. C. Phipps and C. Bonnal, Preparing Satellites for Active Debris Removal and Ranging, in *Proceedings of the 5th International Conference on Optics, Photonics and Lasers (OPAL' 2022)*, 2022, pp. 48-50.

Sensors & Transducers, Vol. 258, Issue 4, July 2022, pp. 31-35

Sensors & Transducers

Published by IFSA Publishing, S. L., 2022

http://www.sensorsportal.com

Propagation of Azimuthally Polarized Bessel-Gaussian Beam through Helical Axicon

[1] Ibrahim G. H. LOQMAN, [1, *] Abdu A. ALKELLY and [1, 2] Hassan T. ALAHSAB

[1] Physics Department, Faculty of Science, Sana'a University, Sana'a, Yemen

[2] Physics Department, Faculty of Applied Science, Dhamar University, Dhamar, Yemen

[*] Tel.: +967777267057

E-mail: a.alkelly@su.edu.ye

Received: 1 June 2022 /Accepted: 5 July 2022 /Published: 29 July 2022

Abstract: Propagation properties of azimuthally polarized Bessel-Gaussian (APBG) beams with non-zero order through a helical axicon (HA) are theoretically investigated. The formula of APBG beams field in the focal region are derived by the vector diffraction theory. Numerical results illustrate that the beam and axicon parameters affect the intensity distribution in the focal region very considerably. Super--long transversely polarized focal depth with different shapes are obtained by choosing appropriate values of parameters. We also observed that a focal shift occurs which depends on both axicon parameter and numerical aperture. We expect that focusing APBG beams by HA can be used in optical trapping.

Keywords: Bessel-Gaussian beam, Azimuthal polarization, Helical axicon, Vector di□raction theory.

1. Introduction

A helical axicon is a hybrid of a spiral phase plate, that is an optical element whose thickness increases azimuthally, and of an axicon [1]. It has attracted researchers' interest due to its unique characteristics and different applications. It is shown that the helical axicon (HA) can be used to transform Gaussian beam and a plane wave into a vortex beam [2, 3]. The HA also has been used to generate Bessel-Gaussian beams of arbitrary order [4], spiraling Bessel beams with adjustable topological charges from Laguerre-Gaussian beam [5], vortex beams [6, 7] and non-di□racting Bessel beam by conversion high-order Laguerre-Gaussian beam [8]. It is found that the topological charge and axicon parameter can alter the focal pattern in the focal region [9, 10]. A general approximate analytical expressions of the Fresnel diffraction of Laguerre–Bessel–Gaussian beam by the HA has been derived analytically based on the stationary phase method [11].

Last decades, high order Bessel–Gaussian beams that propagate with stability in both size and intensity have attracted lots of researchers' attentions due to their extraordinary properties. Such class of beams propagate without divergence, carrying orbital angular momentum with a helical phase fronts and have the property of self-healing [12 - 15]. These properties have propitiated their application in optical trapping [16, 17], optics communication [18] and generating perfect optical vortices [19]. Recently, focusing of polarized Bessel-Gaussian beams which have either pure azimuthal or pure radial polarization had been studied extensively. A needle of strong longitudinal polarized field with long depth of focus and strong intensity has been obtained by focusing a radially polarized Bessel–Gaussian beams with a high numerical aperture lens and a diffractive optical element [20]. In [21], X. Gao et. al. have investigated focusing properties of Bessel–Gaussian beam with radial varying polarization detail. The same group, also, studied the focus shaping of the radially polarized Bessel–Gaussian beam with a sine-azimuthal variation wave front [22]. Multiple intensity rings, dark hollow have been generated by focusing radial varying polarized Bessel–Gaussian beam with radial phase modulation [14]. It is found that radially polarized laser beams have small focuses and non-propagating longitudinal field components; while azimuthally polarized beams have hollow intensity distributions form [17].

By taking into account the fact that focusing Bessel–Gaussian beams are very important in many applications such as optical trapping [17] and the properties of the HA. To the best of our knowledge, the propagation properties of APBG beam through the HA are investigated for the first time in this work. The propagation properties of focused APBG beams such as depth of focus (DOF) and the full width at half maximum (FWHM) by a linear axicon, that is a special case of the HA when the topological charge of a HA p = 0, are also studied. The theoretical model is introduced in section 2. The numerical results are discussed in section 3. In section 4 the conclusion of results is shown.

2. Theoretical Model

The electric field of the APBG beam E(ρ, ϕ), in cylinderical coordinate system (ρ, ϕ, z), at the source plane can be given by

$$\boldsymbol{E}(\rho,\phi) = E(\rho,\phi)\boldsymbol{e_\phi}, \quad (1)$$

where $\boldsymbol{e_\phi}$ is the azimuthal unit vector of the polarized direction and $E(\rho,\phi)$ is the electric field of Bessel-Gaussian beam that is given by [23]

$$E(\rho,\phi) = J_1(\beta\rho)\exp\left(-\frac{\rho^2}{w_0^2}\right)\exp(i\phi), \quad (2)$$

where J_1 is the Bessel function of the first kind of order 1 which is the topological charge of the optical vortex, β is the transverse wave number that indicates the quickness of the fluctuation of Bessel function and w_0 is the beam width. The transmittance of the HA is defined as [6]

$$T = \exp(\mathrm{i}\alpha\rho + ip\phi), \quad (3)$$

where α is the axicon parameter that shows the axicon strength and $p = 0, \pm1, \pm2, \ldots$ is a topological charge of the HA. Based on the variable transformation Eq.3 can be rewritten as [9, 10]:

$$T = \exp\left[i\alpha\rho_b\frac{\rho}{\rho_b} + \mathrm{i}p\phi\right] = \exp\left[i\alpha\rho_b\frac{\rho}{\rho_b} + ip\phi\right] = \exp\left[i\eta\frac{\sin\theta}{NA} + ip\phi\right], \quad (4)$$

where $\eta = \alpha\rho_b$ is the dimensionless axicon parameter, NA is the numerical aperture and θ is the tangential angle with respect to the optical axis as shown in Fig. 1.

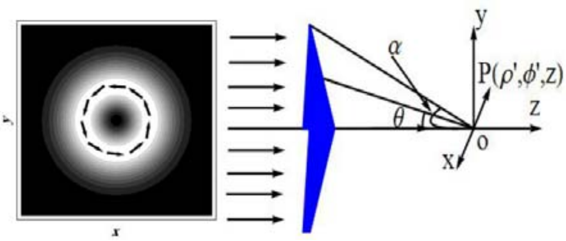

Fig. 1. Scheme for a azimuthally polarized Bessel-Gaussian beam focused by helical axicon.

According to vector diffraction theory, the electric field of APBG beam focused by HA is [24, 25]:

$$\boldsymbol{E}(\rho',\phi',z) = E_{\rho'}\boldsymbol{e_{\rho'}} + E_{\phi'}\boldsymbol{e_{\phi'}} + E_z\boldsymbol{e_z}, \quad (5)$$

where $\boldsymbol{e_{\rho'}}, \boldsymbol{e_{\phi'}}$ and $\boldsymbol{e_z}$ are the radial, azimuthal, and longitudinal unit vectors, respectively. The amplitudes of the three orthogonal components $E_{\rho'}, E_{\phi'}$ and E_z in the focal region are given by

$$\begin{pmatrix} E_{\rho'}(\rho',\phi',z) \\ E_{\phi'}(\rho',\phi',z) \\ E_z(\rho',\phi',z) \end{pmatrix} = -\frac{iA}{\pi}\int_0^{\alpha}\int_0^{2\pi}\sqrt{\cos\theta} * E(\theta,\phi)T(\theta,\phi)\exp[ik(z\cos\theta + \rho'\sin\theta * \cos(\phi-\phi'))] \begin{pmatrix} -\sin\theta\sin(\phi-\phi') \\ \sin\theta\cos(\phi-\phi') \\ 0 \end{pmatrix} d\phi d\theta, \quad (6)$$

where k is the wave number, α = arcsin(NA) is the convergence angle corresponding to the radius of the incident optical aperture. The coordinate system is shown in Fig. 1. In order to simplify calculation process, Eq.2 can be expressed as [26, 27]

$$E(\theta,\phi,0) = J_1\left(\frac{2\beta_1 \sin\theta}{NA}\right)\exp\left[-\left(\frac{\beta_2 \sin\theta}{NA}\right)^2\right]\exp(i\phi), * \cos(\phi-\phi'))] \quad (7)$$

where β_1 and β_2 are the ratios of pupil diameter to the beam diameter.

By substituting Eqs. (4) and (7) into Eq. (6) the three orthogonal component of electric field can be obtained as

$$\begin{pmatrix} E_{\rho'}(\rho',\phi',z) \\ E_{\phi'}(\rho',\phi',z) \\ E_z(\rho',\phi',z) \end{pmatrix} = -\frac{iA}{\pi}\int_0^{\alpha}\int_0^{2\pi}\sqrt{\cos\theta}$$
$$*\exp\left[-\left(\frac{\beta_2\sin\theta}{NA}\right)^2\right] J_1\left(\frac{2\beta_1\sin\theta}{NA}\right)\exp\left[i\eta\frac{\sin\theta}{NA}\right.$$
$$\left.+\exp(i(+1)\varphi)\right]\exp[ik(\rho'\sin\theta\cos(\phi-\phi'))]$$
$$\begin{pmatrix} -\sin\theta\sin(\phi-\phi') \\ \sin\theta\cos(\phi-\phi') \\ 0 \end{pmatrix}\exp[ikzcos\theta]d\phi d\theta. \quad (8)$$

The integration with respect to φ can be accomplished by using the following formula:

$$\int_0^{2\pi}\sin(\phi-\phi')\exp[im\phi+it\cos(\phi-\phi')]d\phi$$
$$= \pi i^m\exp(im\phi')[J_{m+1}(t)+J_{m-1}(t)], \quad (9)$$

and

$$\int_0^{2\pi}\cos(\phi-\phi')\exp[im\phi+it\cos(\phi-\phi')]d\phi$$
$$= \pi i^{m+1}\exp(im\phi')[J_{m+1}(t)-J_{m-1}(t)]. \quad (10)$$

Therefore, the orthogonal components of the output electric field are given by:

$$\begin{pmatrix} E_{\rho'}(\rho',\phi',z) \\ E_{\phi'}(\rho',\phi',z) \\ E_z(\rho',\phi',z) \end{pmatrix} = i^pA\exp(i(p+1)\phi')$$
$$*\int_0^{\alpha}\sqrt{\cos\theta}J_1\left(\frac{2\beta_1\sin\theta}{NA}\right)\exp\left[-\left(\frac{\beta_2\sin\theta}{NA}\right)^2+i\eta\frac{\sin\theta}{NA}+\right.$$
$$\left.ikzcos\theta\right]\begin{pmatrix} -\sin\theta[J_{p+2}(k\rho'sin\theta)+J_p(k\rho'sin\theta)] \\ i\sin\theta[J_{p+2}(k\rho'sin\theta)-J_p(k\rho'sin\theta)] \\ 0 \end{pmatrix}d\theta. \quad (11)$$

The optical intensity is proportional to the modulus square of Eq. 5.

3. Numerical Calculation and Discussion

In this section some numerical calculation will be carried out in order to obtain the properties of propagation APBG beam through helical axicon depending on Eq. 11. It is noticeable that the integral over the parameter θ could not accomplished analytically; therefore, the numerical integration will be used. In our calculation, we consider A equal unit one and $\lambda = 632.8$nm and the distance unit in figures in this work is the wavelength of the incident beam in vacuum.

Fig. 2 illustrates the intensity distribution of APBG beam with HA for different axicon parameter $\eta = 0, \eta = 2, \eta = 4, \eta = 6, \eta = -2$ and $\eta = -4$ under condition of $\beta_1 = 2$, $\beta_2 = 1$, $p = 1$, and $NA = 0.95$. This figure shows that the intensity distribution vary with respect to axicon parameter. It is clearly shown that the focal hole shape still constant as the axicon parameter changed and the intensity distribution is symmetry about the z axis. For $\eta = 0$ as it is shown in Fig. 2 (a) the focal region is symmetry about z and its center is at $z = 0$. In addition, it can be seen from Fig. 2 (b-d) the generated focal hole region shifts away from the HA on increasing the positive value of the axicon parameter η. In the other hand, the generated focal hole in the focal region shifts toward the HA on decreasing the negative value the axicon parameter as it is shown in Fig. 2 (e and f) that are for $\eta = -2$ and $\eta = -4$, that indicate focal shift phenomenon occurs that means the movement of the center of focal hole. It can be concluded that different HA different focal hole regions for the same incident beam.

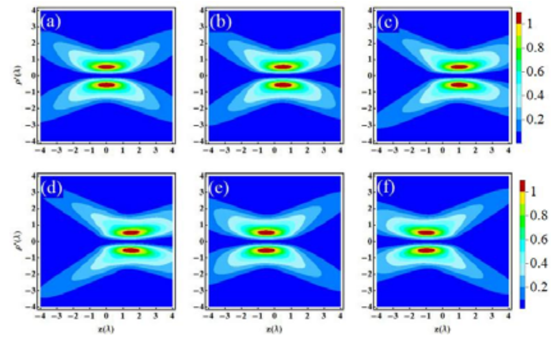

Fig. 2. Intensity distribution of APBG beam with HA under condition $\beta_1 = 2$, $\beta_2 = 1$, $p = 1$, $NA = 0.95$ and (a) $\eta = 0$, (b) $\eta = 2$, (c) $\eta = 4$, (d)$\eta = 6$, (e) $\eta = -2$, (f) $\eta = -4$, respectively.

Fig. 3 exhibits the intensity distribution of APBG beam with a HA for positive and negative different values of topological charge under condition of $\eta = 4$, $\beta_1 = 2$, $\beta_2 = 1$, and $NA = 0.95$. It is shown from Fig. 3 (a and f) that the focused APBGB with $p = 0$ and -2 are not hollow and have peaks on the optical axes due to the presence of J_0 that is found in the integrand for both $p = 0$ and -2. In the other hand, the focal hole region is constructed for $p \neq 0$ and -2 as can be seen in Fig. 3(b, c, d and e). The radius of the focal hole increases as the topological charge either positively increase or negatively decrease. By comparing Fig. 3 (b with e) and Fig. 3 (d with g) it is found that the focal hole region is longer and have smaller radius for negative values of p than positive values. It can be conclude that the HA changes the topological charge of the incident beams and convert it to a non-vortex beam [8, 7].

Now, let the parameters β_1 and β_2 vary to show how the focal hole region change. In Fig. 4 the parameter β_1 increase from 1 to 3.5 for $\beta_2 = 1$ and in Fig. 4 the parameter β_2 increase from 1.5 to 2.5 for $\beta_1 = 3$ the other parameters are $\eta = 2$, $NA = 0.95$, and $p = 1$ for both of them. It is obviously shown that the shape of the focal hole region in these two figures have changed considerably and some novel focal hole patterns are appear including dark hollow focus, multiple intensity ring that can be used to construct optical traps. In addition, the focal hole region shift is not related to the parameters β_1 and β_2 as it is shown from Figs. 4 and 5. In addition, the position of the maximum intensity value change as the values of both parameters β_1 and β_2 change with forming different focal region shapes. Therefore, they can affect the focal pattern considerably and produce some novel focal hole regions that can be used in optical trapping.

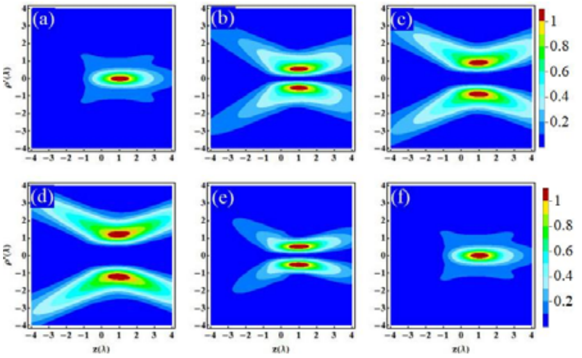

Fig. 3. Intensity distribution of APBG beam with HA under condition $\beta_1 = 2, \beta_2 = 1, \eta = 4, NA = 0.95$ and (a) $p = 0$, (b) $p = 1$, (c) $p = 2$, (d)$p = 3$, (e) $p = -1$ and (f) $p = -2$, respectively.

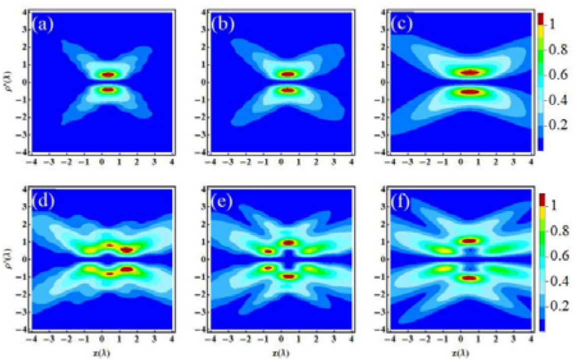

Fig. 4. Intensity distribution of APBG beam with HA under condition $\eta = 2$, $NA = 0.95$, $p = 1$,$\beta_2 = 1$ and (a) $\beta_1 = 1$, (b) $\beta_1 = 1.5$, (c) $\beta_1 = 2$, (d) $\beta_1 = 2.5$, (e)$\beta_1 = 3$, (f) $\beta_1 = 3.5$, respectively.

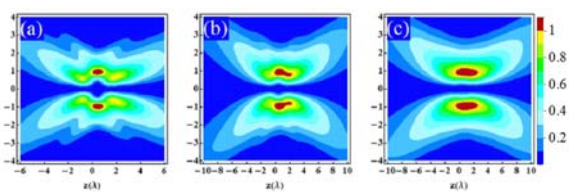

Fig. 5. Intensity distribution of APBG beam with HA under condition $\eta = 4$, $NA = 0.95$ $\beta_1 = 3$ and (a) $\beta_2 = 1.5$, (b) $\beta_2 = 2$, (c) $\beta_2 = 2.5$, respectively.

The intensity distribution of APBG beams with different values of numerical aperture with $p = 1$ and $p = 0$, that is corresponding to a linear axicon, under condition $\eta = 2$, $\beta_1 = 3$ and $\beta_2 = 3$ are shown in Fig. 6. It can be seen that the intensity distribution in the focal region strongly depend on both the nume rical aperture and the topological charge. While a transversely polarized focal hole is formed with $p = 1$ an extended focal spot is formed with $p = 0$. The focal depth considerably extend as the numerical aperture decrease and the focal shift increase, also, that are coincide with our previous work [28]. A super–long focal tube is obtained from focusing APBG beams with small values of numerical aperture. The dependence of both DOF and FWHM of focused APBG beam by a linear axicon on the numerical aperture are illustrated in Fig. 7 under condition of $\eta = 2$, $\beta_1 = 3$, $\beta_2 = 3$, and $NA = 0.95$. It is clearly shown that the depth of focus increases considerably as the NA decreases. The depth of focus equal 48.9λ and 38.6λ for $NA = 0.40$ and $NA = 0.45$, respectively. Moreover, the FWHM is also extend as the numerical aperture decrease.

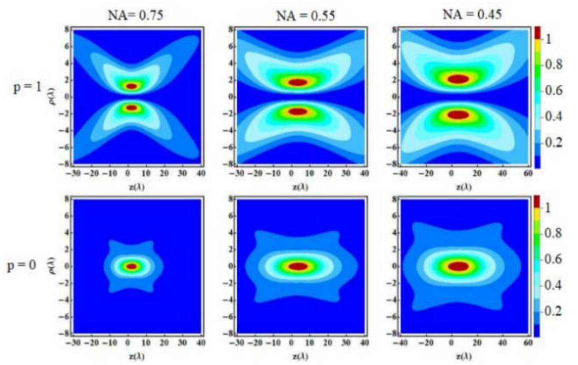

Fig. 6. Intensity distribution of APBG beam with HA under condition $\eta = 2$, $\beta_1 = 3$ and $\beta_2 = 3$ with $p = 0$ and $p = 1$.

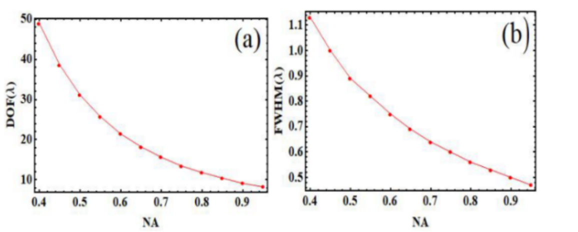

Fig. 7. Depth of focus (DOF) and the full width at half maximum (FWHM) of a focused APBG beam with HA under condition $\eta = 2$, $\beta_1 = 3$, $\beta_2 = 3$ and $p = 0$ that is corresponding to a linear axicon.

4. Conclusions

In summary, by using the vector diffraction theory propagation properties of the azimuthally polarized Bessel-Gaussian beam (APBGB) through helical axicon is numerically investigated. Our numerical results clearly show that the intensity distribution in the focal region of the APBGB can be adjusted considerably by axicon parameter, topological charge of the spiral phase, and beam parameters. A long focal tube has been obtained. We suggest that focusing of APBGB by HA may find application in optical trapping.

References

[1]. S. Khonina, V. Kotlyar, V. Soifer, M. Shinkaryev, G. Uspleniev. Trochoson, *Optics Communications,* Vol. 91, 1992, pp. 158–162.

[2]. V. V. Kotlyar, A. A. Kovalev, R. V. Skidanov, O. Y. Moiseev, V. A. Soifer, Di□raction of a finite-radius plane wave and a gaussian beam by a helical axicon and a spiral phase plate, *J. Opt. Soc. Am. A*, Vol. 24, Issue 7, 2007, pp. 1955–1964.

[3]. M. Beijersbergen, R. Coerwinkel, M. Kristensen, J. Woerdman, Helical-wavefront laser beams produced with a spiral phaseplate, *Optics Communications,* Vol. 112, 1994, pp. 321–327.

[4]. V. Arriz´on, U. Ruiz, D. Aguirre-Olivas, D. S´anchez-de-la Llave, A. S. Ostrovsky, Comparing e□ciency and accuracy of the kinoform and the helical axicon as bessel–gauss beam generators, *J. Opt. Soc. Am. A*, Vol. 31, Issue 3, 2014, pp. 487–492.

[5]. S. Qiong-Ge, Z. Ke-Ya, F. Guang-Yu, L. Zheng-Jun, L. Shu-Tian, Generalization and propagation of spiraling Bessel beams with a helical axicon, *Chinese Physics B,* Vol. 21, Issue 1, 2012, p. 014208.

[6]. V. Kotlyar, A. Kovalev, V. Soifer, C. S. Tuvey, J. A. Davis, Sidelobe contrast reduction for optical vortex beams using a helical axicon, *Optics Letters*, Vol. 32, Issue 8, 2007, pp. 921–923.

[7]. S. Topuzoski, L. Janicijevic, Diffraction of laguerre-gaussian beam by a helical axicon, *Acta Physica Polonica-Series A General Physics,* Vol. 9, Issue 4, 2009, pp. 557.

[8]. S. Topuzoski, L. Janicijevic, Conversion of high-order Laguerre–Gaussian beams into Bessel beams of increased, reduced or zeroth order by use of a helical axicon, *Optics Communications,* Vol. 282, Issue 17, 2009, pp. 3426–3432.

[9]. X. Dong, T. Geng, S. Zhuang, Focusing properties of hyperbolic-cosine-Gaussian beams combining a helical axicon, *Optik,* Vol. 124, Issue 18, 2013, pp. 3422–3426.

[10]. G. Wang, Y. Miao, Q. Zhan, G. Sui, R. Zhang, Focusing of linearly polarized Lorentz-Gaussian beam with helical axicon, *Optik,* Vol. 130, Issue 2017, pp. 266–272.

[11]. F. Saad, Z. Hricha, M. Khouilid, A. Belafhal, A theoretical study of the Fresnel diffraction of Laguerre-Bessel-Gaussian beam by a helical axicon, *Optik,* Vol. 149, 2017, pp. 416–422.

[12]. S. Vyas, Y. Kozawa, S. Sato, Self-healing of tightly focused scalar and vector Bessel–Gauss beams at the focal plane, *J. Opt. Soc. Am. A,* Vol. 28, Issue 5, 2011, pp. 837–843.

[13]. S. Zhao, W. Zhang, L. Wang, W. Li, L. Gong, W. Cheng, H. Chen, J. Gruska, Propagation and self-healing properties of Bessel-Gaussian beam carrying orbital angular momentum in an underwater environment, *Scientific Reports,* Vol. 9, Issue 1, 2019, pp. 1–8.

[14]. B. Wu, X. Zeng, Y. Miao, Y. Fan, X. Gao, S. Zhuang, Focal shift of radial varying polarized Bessel-Gauss beam with radial phase modulation, *Optik,* Vol. 157, 2018, pp. 675–683.

[15]. G. Wu, F. Wang, Y. Cai, Generation and self-healing of a radially polarized Bessel-Gauss beam, *Physical Review A,* Vol. 89, Issue 4, 2014, pp. 043807.

[16]. G. Volpe, G. P. Singh, D. Petrov, Optical tweezers with cylindrical vector beams produced by optical fibers, in: Optical Trapping and Optical Micromanipulation, *International Society for Optics and Photonics*, Vol. 5514, 2004, pp. 283–292.

[17]. F. Wu, B. Zhang, Z. Liu, Y. Tang, N. Zhang, Optical trapping forces of a focused azimuthally polarized Bessel-Gaussian beam on a double-layered sphere, *Optics Communications,* Vol. 405, 2017, pp. 96–100.

[18]. F. Zhu, S. Huang, W. Shao, J. Zhang, M. Chen, W. Zhang, J. Zeng, Free-space optical communication link using perfect vortex beams carrying orbital angular momentum (oam), *Optics Communications,* Vol. 396, 2017, pp. 50–57.

[19]. M. K. Karahroudi, B. Parmoon, M. Qasemi, A. Mobashery, H. Saghafifar, Generation of perfect optical vortices using a Bessel–Gaussian beam diffracted by curved fork grating, *Applied Optics,* Vol. 56, Issue 21, 2017, pp. 5817–5823.

[20]. K. Huang, P. Shi, X.-l. Kang, X. Zhang, Y.-P. Li, Design of doe for generating a needle of a strong longitudinally polarized field, *Optics Letters,* Vol. 35, Issue 7, 2010, pp. 965–967.

[21]. X. Gao, R. Fu, H. Shen, X. Dong, T. Geng, S. Zhuang, Focus shaping of Bessel–Gauss beam with radial varying polarization, *Optica Applicata,* Vol. 42, Issue 3, 2012, pp. 481–491.

[22]. X. Gao, D. Zhang, T. Mei, R. Fu, S. Zhuang, Focus shaping of the radially polarized Bessel–Gauss beam with a sine-azimuthal variation wavefront, *Optica Applicata,* Vol. 43, Issue 3, 2013, pp. 567-582.

[23]. F. Gori, G. Guattari, C. Padovani, Bessel-Gauss beams, *Optics Communications,* Vol. 64, Issue 6, 1987, pp. 491–495.

[24]. K. S. Youngworth, T. G. Brown, Focusing of high numerical aperture cylindrical-vector beams, *Optics Express,* Vol. 7, Issue 2, 2000, pp. 77–87.

[25]. S. Sato, Y. Kozawa, Hollow vortex beams, *J. Opt. Soc. Am. A,* Vol. 26, Issue 1, 2009, pp. 142–146.

[26]. E. Y. Yew, C. J. Sheppard, Tight focusing of radially polarized Gaussian and Bessel-Gauss beams, *Optics Letters,* Vol. 32, Issue 23, 2007, pp. 3417–3419.

[27]. X. Gao, S. Hu, J.-S. Li, Z.-H. Ding, H.-M. Guo, S.-L. Zhuang, et al., Tunable optical gradient trap by radial varying polarization Bessel–Gauss beam, *Journal of Biomedical Science and Engineering,* Vol. 3, Issue 3, 2010, pp. 304–307.

[28]. A. A. Alkelly, I. G. H. Loqman, H.-M. H. T. Al-Ahsab, Focus shaping of cylindrically polarized vortex beams by a linear axicon, *Electronic Journal of University of Aden for Basic and Applied Sciences,* Vol. 2, Issue 4, 2021, pp. 145–150.

Sensors & Transducers, Vol. 258, Issue 4, July 2022, pp. 36-41

Sensors & Transducers
Published by IFSA Publishing, S. L., 2022
http://www.sensorsportal.com

Study of Polycarbonate Wettability and its Antibacterial Properties after Excimer Laser Irradiation at the Ablation Threshold Fluence

[1, *] Sahar Sohrabi, [2] Hedieh Pazokian, [1] Bijan Ghafary, [1] Mahmood Mollabashi and [2] Mohsen Montazeralghaem

[1] Iran University of Science and Technology, Physics Department, Tehran, Iran
[2] Photonics and Quantum Technology Research School, Nuclear Science and Technology Research Institute, Tehran, Iran
[1] Tel.: +989194325260
[*] E-mail: s.sohrabiiust@gmail.com

Received: 2 June 2022 /Accepted: 4 July 2022 /Published: 29 July 2022

Abstract: Wettability is reported to be one of the most important factors in bacterial attachment into the surface. Superhydrophobic surfaces show the lowest bacterial adhesion. In this paper, effect of an excimer laser irradiation at the ablation threshold fluence with different number of pulses on the wettability and antibacterial properties of polycarbonate samples was investigated. Sessile drop method and gram staining technique were used for water contact angle measurement and adhered bacteria identification respectively. Laser irradiation on the polycarbonate surface, cause intense changes in its wettability. High number of laser pulses at the ablation threshold fluence, followed by suitable hierarchical micro-nano structures fabrication on the surface, causes super water repellent surface fabrication. This fabricated surface shows superhydrophobicity and antibacterial properties and can be used in many applications such as medical devices, water and food industry. Field Emission Scanning Electron Microscopy was used for investigating the morphology of the superhydrophobic fabricated polycarbonate and to ensure adhered bacteria rate of the superhydrophobic sample.

Keywords: Antibacterial properties, Excimer laser, Polycarbonate, Superhydrophobicity, Wettability.

1. Introduction

Colonization and bacterial attachment on the surface of medical devices cause bacterial infections and threats to human health [1]. As the use of antibiotics, there are several approaches to kill the bacteria directly [2], but increasing the bacterial resistance to antibiotics followed by the emergence of new strains of drug-resistance bacteria, reduces the tendency to use these methods [3].

On the other hand, there are other techniques to prevent bacterial infections such as some metal particles using. Metal surfaces such as silver or copper have shown antibacterial efficacies that may control bacterial infections [4], but using this method leading to irreversible destructive effects such as DNA molecules damage [5].

Using new methods based on preventing the initial adhesion of bacteria to the surface, does not have the destructive effects of previous methods and also the antibacterial effect is more lasting. These surfaces can reduce the adhesion force between bacteria cells and the surface to enable the easy removal of bacteria before a biofilm formation [6].

Antibacterial surfaces have attracted scientists attention in the last decades [7, 8] due to their extensive applications such as industrial equipment, human health, food and water industry. As was mentioned in the previous paragraph, these surfaces prevent the initial bacterial attachment to the surface and subsequently biofilm formation [9].

Multiple physical aspects of the material including wettability, roughness, surface charge and energy have been considered to influence on the bacterial adhesion rate, but wettability is reported to be the most relevant parameter for bacterial adhesion control [10]. Superhydrophobic surfaces have been reported to show the lowest adhered bacteria due to their micro-nano structures [11]. There are several methods for superhydrophobic surfaces fabrication including chemical etching [12], solution immersion [13] and laser processing [14].

Laser irradiation can change the surface wettability due to the chemical changes and micro/nano structures formation on the surface and is one of the most effective techniques for superhydrophobic surfaces fabrication. Numerous articles have been published investigating the effect of the laser irradiation at fluences of above the ablation threshold on the wettability of the sample [15]. In this paper, effect of an excimer laser irradiation of polycarbonate at the ablation threshold fluence on its wettability is investigated. Due to laser processing, at these fluences and with high number of pulses, the surface is changed to superhydrophobic one. Finally, the bacterial adhesion rate on the irradiated sample is tested.

2. Experimental Method

2.1. Experimental Work

Polycarbonate is one of the most widely used polymers in food and medical industries. For example, this polymer has been used in blood filters and blood reservoirs for more than 20 years. In addition, this polymer is also used in food packaging containers. These applications are directly related to human health. Therefore, it seems that antibacterial polycarbonate fabrication is very essential.

Polycarbonate samples with the thickness of 1mm were cut into length and width of 1cm × 1cm. The samples were washed with water and alcohol to be cleaned before laser processing. The UV-Vis spectrum of the selected polycarbonate is shown in Fig. 1.

As it can be seen from the spectrum, PC has high absorption at the UV range of the spectrum.

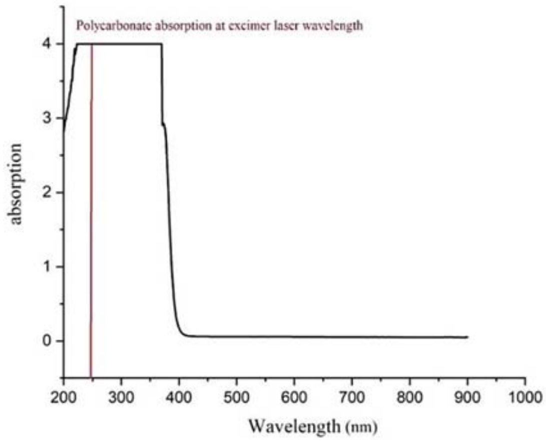

Fig. 1. UV-Vis spectrum of polycarbonate.

The single pulse laser ablation threshold can be obtained from the extrapolation of the graph of laser ablation rate vs laser fluence [16]. The fluence for the single pulse ablation threshold of PC samples in 248 nm was obtained to be about 40 mJ/cm^2. For investigating the effect of the laser irradiation on the polycarbonate wettability, samples were irradiated by a pulsed KrF laser with 25 ns duration and 248 nm wavelength at the fluence of 35 mJ/cm^2 (very close to the ablation threshold) with different number of pulses. The experimental setup is shown in Fig. 2.

The contact angle of the pristine and irradiated samples were realized by sessile drop method. Field Emission Scanning Electron Microscopy (FESEM) was used for investigating the changes in the superhydrophobic fabricated surface's morphology.

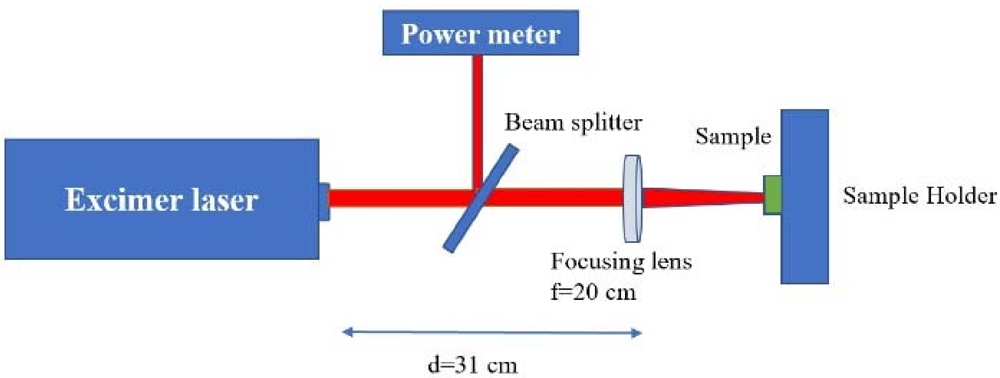

Fig. 2. Scheme of the experimental setup.

2.2. Bacterial Retention

E-Coli bacteria culture was inoculated into 4 mL LB and then incubated at 37 °C to an OD_{600} of 0.5. The culture was diluted 1:3 in sterile phosphate buffer solution (PBS). 500 microliters of diluted bacteria cultures were added to each well of polycarbonate samples. After washing with PBS, bacteria were fixed on the samples with 4 % paraformaldehyde in PBS for 30 min at room temperature and then Samples were rinsed with PBS. Finally, Gram staining was done.

One of the practical methods for identification of bacteria, is gram staining. Bacteria are classified into two categories based on their colour after gram staining test. Gram-negative and gram-positive bacteria are violet and red colour after gram staining.

In this paper, the superhydrophobic fabricated sample and the pristine were tested for E-Coli bacteria adhesion with gram staining method. E-Coli bacteria is gram-negative and can be identified easily in optical microscope due to its violet colour after bacteria culture and gram staining test.

3. Results

3.1. Wettability

Fig. 3 shows the changes in water contact angle of the samples irradiated at the fluence of 35 mJ/cm^2 and with different number of pulses.

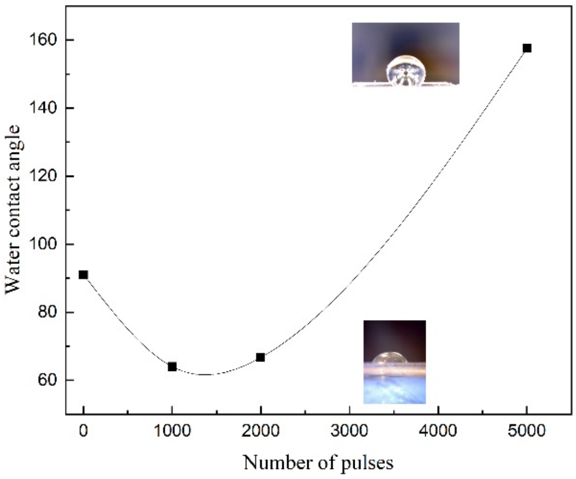

Fig. 3. Water contact angle of the irradiated polycarbonate samples at the fluence of 35 mJ/cm^2 with different number of pulses.

As it can be understood from the figure, following irradiation of the samples at this fluence with 1000 and 2000 number of pulses, the surface become hydrophilic, while the irradiated polycarbonate shows superhydrophobic behavior with 5000 pulses of irradiation.

3.2. Bacterial Adhesion Test

As was mentioned in Section 2.2, after bacteria culture, gram staining method was used for the superhydrophobic fabricated sample and the pristine. All the samples with bacterial culture and gram staining tests, were washed with phosphate buffer solution (PBS) before taking microscopic images. Therefore, only adhered E-Coli bacteria can be seen in the microscopic images.

Fig. 4 shows the microscopic images of these samples for E-Coli bacteria identification. As it can be seen from the figure, adhered E-Coli bacteria can be seen easily on the pristine sample while almost no bacteria can be identified on the superhydrophobic one. This means that the superhydrophobic fabricated sample is also antibacterial. Water droplet, can be slipped easily on the superhydrophobic surfaces. So these surfaces are self-cleaning. With PBS washing, bacteria that were on the surface but did not adhere to it, could easily be removed. No E-Coli bacteria can be seen in the microscopic image of the sample irradiated with 5000 number of pulses. So the adhesion force between the superhydrophobic surface and E-Coli bacteria is so low and bacteria can not adhere on the surface. In addition, if there is any bacteria on the surface, it can be removed easily by washing.

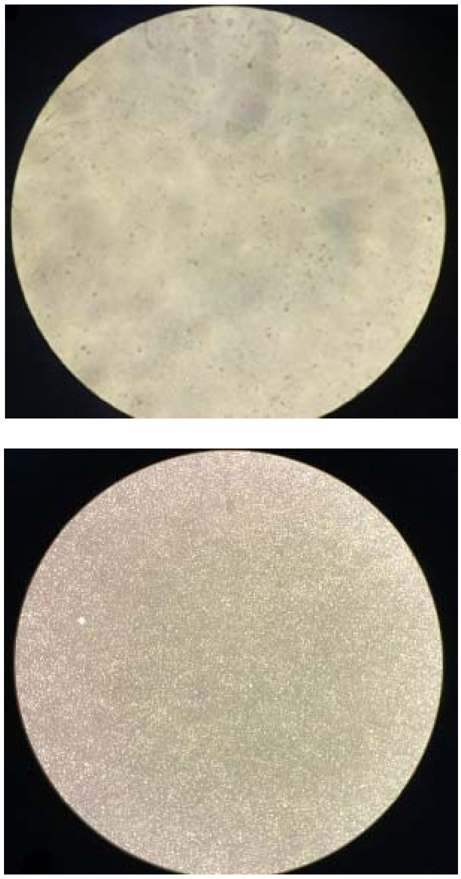

Fig. 4. Microscopic images of up untreated and down the sample irradiated at the fluence of 35 mJ/cm^2 with 5000 number of pulses. The microscopic images are one hundred times larger than the original.

3.3. Morphology

Fig. 5 shows the FESEM images of the irradiated sample with 5000 pulses, as a superhydrophobic specimen, with different magnifications. These images were taken after the bacteria culture to ensure that no bacteria is adhered to the superhydrophobic sample.

As it can be understood from the figure, micro-nano scale structures are formed on the surface following irradiation with 5000 pulses at fluence of 35 mJ/cm^2. Fig. 5 (a) shows the microstructures formation on the irradiated polycarbonate with 5000 pulses and (b) shows the nanostructures formation on the microstructures with higher magnification. As it can be seen from the image, nano spheres with diameter of about 60-90 nanometres are formed on the whole parts of the microstructures. This structure are similar to one was formed on the polymers following irradiation with an excimer laser at near the ablation threshold fluence [17, 18].

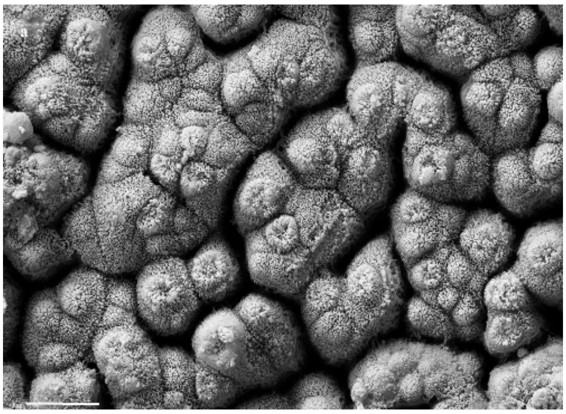

Fig.5. FESEM images of the sample irradiated at the fluence of 35 mJ/cm^2 with 5000 number of pulses after bacterial test at different magnification. Marked scale bar is about a) 4 micron, and b) 400 nm

4. Discussion

Laser irradiation of polymers at the ambient with nanosecond laser leads to different chemical and morphological changes based on the laser fluence regime. Material removal, morphological changes and micro scale structures formation are expected to occur at the fluences above the ablation threshold. In this case, the surface hydrophobicity is expected to increase. At the fluences below and close to the ablation threshold, chemical modifications and polar group's formation are occurred and these changes can turn the surface into the hydrophilic one, according to number of laser pulses. It is important to note that the number of laser pulses is the main factor in laser-matter interaction at the fluence below and close to the ablation threshold. At this fluence, chemical changes are occurred; but as it was mentioned, the intended fluence is so close to the ablation threshold and with high number of pulses, formation of nano size structures is expected [19].

Following irradiation of the sample with 1000 and 2000 number of pulses, chemical changes are occurred followed by polar group's formation as was mentioned in the previous paragraph. These polar groups may interact with H_2O molecule and cause surface to become hydrophilic.

With higher number of pulses as 5000 at this fluence, the energy of the laser pulses cause the creation of the structure and nano scale structures can be formed on the surface. 1000 and 2000 number of pulses are not enough for suitable nanostructures formation. Cassie-Baxter model predict that on the surfaces with micro/nano structures, air pockets can be entrapped in the structures and the surface shows superhydrophobicity behaviour [20].

Fig. 5 shows the hierarchical structures formation on the irradiated PC with 5000 number of pulses. Hierarchical structures formation on the surface is supposed to be one of the best approaches for artificial superhydrophobic surfaces fabrication [21]. In these surfaces, air is entrapped between the structures and the water droplet will be in contact with gas phase instead of the solid [22]. So the water contact angle of these surfaces will be so high and they have potential to be superhydrophobic surfaces. Air trapping in-between the fabricated structures is the main reason for their superhydrophobicity. Since no bacteria can be seen in these FESEM images, the superhydrophobic fabricated polycarbonate have antibacterial properties.

Both hydrophilic and superhydrophobic surfaces are used in many industries due to their vast applications. Hydrophilic surfaces can be used in biomedical, heat pipes and many other applications [23], while research has shown anti-biofouling, antibacterial and self-cleaning properties of superhydrophobic surfaces [24, 25]. So based on a specific application, the desired surface wettability can be obtained using a laser treatment method.

Numerous articles have reported that bacteria prefer to adhere to the solid phase rather than the gas [26, 27]. As was mentioned before, air trapping in the fabricated structures occurs. So bacteria will contact with the air as a gas phase instead of the surface as a solid phase. So bacterial adhesion on this surface will be at the lowest level and this surface is antibacterial one.

5. Conclusions

Due to the increasing bacterial resistance to antibiotics and the fact that the development of new strains of drug-resistant bacteria is expected to be faster than the production of new drugs in the next few years, the development of antibacterial surfaces that prevent the bacterium from initial adhesion to the surface has received much attention in the last decade. Superhydrophobic surfaces are reported to be the antibacterial ones. There are many approaches for superhydrophobic surfaces fabrication but laser treatment, as a simple and single-step method which can form suitable structures on the surface, is considered to be one of the best methods for this purpose. In this paper, effect of laser treatment of polycarbonate on its wettability and antibacterial properties was investigated. The polycarbonate samples were irradiated with an excimer laser at the ablation threshold fluence with different number of pulses. Chemical modifications such as surface carbonization and polar group's formation, as well as morphological changes including micro/nano structures formation are the reasons for wettability modifications of the irradiated samples. The number of pulses is the most important factor affect the wettability at the fluence below and near the ablation threshold. With 1000 and 2000 number of pulses, polar groups are formed on the surface which cause the surface become hydrophilic, while with 5000 number of pulses, nanostructures are formed on the irradiated surface and the surface is changed into the superhydrophobic one. Therefore, according to the experimental results, it is clear that the wettability in this fluence can be changed drastically with the number of laser pulses.

FESEM of the irradiated sample with 5000 pulses, shows the nanostructures formation on the surface. Air-trapping between these structures is the main reason for superhydrophobicity of this sample.

Bacterial adhesion test was done for the pristine and the superhydrophobic fabricated surface. After PBS washing, microscopic images of the surfaces were taken. According to the images, no adhered bacteria can be seen on the superhydrophobic surface, while many adhered bacteria are on the pristine polycarbonate. Bacteria prefer to adhere to the solid phase rather than the gas. Therefore, since there is air between the structures created on the superhydrophobic surface based on the Cassie-Baxter model, bacteria have little contact with the solid phase and most of the contact is with the gas phase. Therefore, this surface has antibacterial properties.

Finally, in this research, superhydrophobic antibacterial polycarbonate is fabricated using an excimer laser treatment. This fabricated sample can be used in many industries such as food, water and medicine.

References

[1]. K. Seku, K. K. Kumar, G. Narasimha, and G. B. Reddy, Bio-mediated synthesis of silver nanoparticles via microwave-assisted technique and their biological applications, in Green Synthesis of Silver Nanomaterials, *Elsevier*, 2022, pp. 149-188.

[2]. Y. Yuan, M. P. Hays, P. R. Hardwidge, and J. Kim, Surface characteristics influencing bacterial adhesion to polymeric substrates, *RSC Advances,* Vol. 7, No. 23, 2017, pp. 14254-14261.

[3]. T. Flak *et al.*, Novel Antibacterial Modification of Polycarbonate for Increment Prototyping in Medicine, *Materials,* Vol. 14, No. 16, 2021, p. 4725.

[4]. M. Y. Vaidya, A. J. McBain, J. A. Butler, C. E. Banks, and K. A. Whitehead, Antimicrobial efficacy and synergy of metal ions against Enterococcus faecium, Klebsiella pneumoniae and Acinetobacter baumannii in planktonic and biofilm phenotypes, *Scientific Reports,* Vol. 7, No. 1, 2017, pp. 1-9.

[5]. G. V. Vimbela, S. M. Ngo, C. Fraze, L. Yang, and D. A. Stout, Antibacterial properties and toxicity from metallic nanomaterials, *International Journal of Nanomedicine,* Vol. 12, 2017, p. 3941.

[6]. C. Adlhart *et al.*, Surface modifications for antimicrobial effects in the healthcare setting: A critical overview, *Journal of Hospital Infection,* Vol. 99, No. 3, 2018, pp. 239-249.

[7]. K. Schwibbert, F. Menzel, N. Epperlein, J. Bonse, and J. Krüger, Bacterial adhesion on femtosecond laser-modified polyethylene, *Materials,* Vol. 12, No. 19, 2019, p. 3107.

[8]. X. Yang, J. Hou, Y. Tian, J. Zhao, Q. Sun, and S. Zhou, Antibacterial surfaces: Strategies and applications, *Science China Technological Sciences*, 2022, pp. 1-11.

[9]. H. Qiu *et al.*, The mechanisms and the applications of antibacterial polymers in surface modification on medical devices, *Frontiers in Bioengineering and Biotechnology*, 2020, p. 910.

[10]. S. Sohrabi, H. Pazokian, B. Ghfary, M. Mollabashi, M. Montazeralghaem, Superhydrophobic Polycarbonate Fabrication for Antibacterial Applications, in *Proceedings of the 5th International Conference on Optics, Photonics and Lasers*, Canary Islands, Spain, 2022, pp 7-8.

[11]. X. Zhang, L. Wang, and E. Levänen, Superhydrophobic surfaces for the reduction of bacterial adhesion, *Rsc Advances,* Vol. 3, No. 30, 2013, pp. 12003-12020.

[12]. A. Esmaeilirad, M. V. Rukosuyev, M. B. Jun, and F. C. van Veggel, A cost-effective method to create physically and thermally stable and storable super-hydrophobic aluminum alloy surfaces, *Surface and Coatings Technology,* Vol. 285, 2016, pp. 227-234.

[13]. J. Xu, J. Xu, Y. Cao, X. Ji, and Y. Yan, Fabrication of non-flaking, superhydrophobic surfaces using a one-step solution-immersion process on copper foams, *Applied Surface Science,* Vol. 286, 2013, pp. 220-227.

[14]. J. Yong *et al.*, Stable superhydrophobic surface with hierarchical mesh-porous structure fabricated by a femtosecond laser, *Applied Physics A,* Vol. 111, No. 1, 2013, pp. 243-249.

[15]. S. Sohrabi, H. Pazokian, B. Ghafary, and M. Mollabashi, Superhydrophobic-antibacterial polycarbonate fabrication using excimer laser treatment, *Optik*, 2022, p. 169377.

[16]. H. Pazokian, M. Vesal, S. Sohrabi, and M. Mollabashi, Fabrication of multiscale structures on polymethylmethacrylate following pulsed CO_2 laser irradiation, *Optical Engineering,* Vol. 57, No. 12, 2018, p. 125103.

[17]. H. Pazokian, A. Selimis, E. Stratakis, M. Mollabashi, J. Barzin, and S. Jelvani, KrF laser ablation of a polyethersulfone film: effect of pulse duration on structure formation, *Applied Surface Science,* Vol. 258, No. 1, 2011, pp. 169-175.

[18]. H. Pazokian *et al.*, Tailoring the wetting properties of polymers from highly hydrophilic to superhydrophobic using UV laser pulses, *Journal of Micromechanics and Microengineering,* Vol. 22, No. 3, 2012, p. 035001.

[19]. C. T. Salazar, M. L. Azcárate, and C. A. Rinaldi, Nanostructuring of material surfaces by laser ablation, *Radiation Effects in Materials*, 2016, p. 431.

[20]. H. Y. Erbil and C. E. Cansoy, Range of applicability of the Wenzel and Cassie − Baxter equations for superhydrophobic surfaces, *Langmuir,* Vol. 25, No. 24, 2009, pp. 14135-14145.

[21]. Y. Lee, S. H. Park, K. B. Kim, and J. K. Lee, Fabrication of hierarchical structures on a polymer surface to mimic natural superhydrophobic surfaces, *Advanced Materials,* Vol. 19, No. 17, 2007, pp. 2330-2335.

[22]. Z. Chang and Y. Lu, Fabrication of superhydrophobic surfaces with Cassie-Baxter state, *Journal of Dispersion Science and Technology*, 2020, pp. 1-13.

[23]. D. Ahmad, I. van den Boogaert, J. Miller, R. Presswell, and H. Jouhara, Hydrophilic and hydrophobic materials and their applications, *Energy Sources, Part A: Recovery, Utilization, and Environmental Effects,* Vol. 40, No. 22, 2018, pp. 2686-2725.

[24]. G. B. Hwang, K. Page, A. Patir, S. P. Nair, E. Allan, and I. P. Parkin, The anti-biofouling properties of superhydrophobic surfaces are short-lived, *ACS Nano,* Vol. 12, No. 6, 2018, pp. 6050-6058.

[25]. H. Okkay, S. Satı, and U. Cengiz, Mechanically stable superhydrophilic antifog surface by microwave assisted sol-gel method, *Journal of the Taiwan Institute of Chemical Engineers,* Vol. 120, 2021, pp. 360-367.

[26]. T. R. Garrett, M. Bhakoo, and Z. Zhang, Bacterial adhesion and biofilms on surfaces, *Progress in Natural Science,* Vol. 18, No. 9, 2008, pp. 1049-1056.

[27]. M. van Loosdrecht, J. Lyklema, W. Norde, and A. J. Zehnder, Bacterial adhesion: a physicochemical approach, *Microbial Ecology,* Vol. 17, No. 1, 1989, pp. 1-15.

Published by International Frequency Sensor Association (IFSA) Publishing, S. L., 2022 (http://www.sensorsportal.com).

Aims and Scope

Sensors & Transducers is established, international, peer-reviewed, open access journal (print and electronic). It provides the best platform for the researchers and scientist worldwide to exchange their latest findings and results in science and technology of physical, chemical sensors and biosensors. The journal publishes original results of scientific and research works related to strategic and applied studies in all aspects of sensors: reviews, regular research and application specific papers, and short notes. In comparison with other sensors related journals, which are mainly focused on technological aspects and sensing principles, the *Sensors & Transducers* significantly contributes in areas, which are not adequately addressed in other journals, namely: frequency (period), duty-cycle, time-interval, PWM, phase-shift, pulse number output sensors and transducers; sensor systems; digital, smart, intelligent sensors and systems designs; signal processing and ADC in sensor systems; advanced sensor fusion; sensor networks; applications, etc. By this way the journal significantly enriches the appropriate databases of knowledge.

Sensors & Transducers journal has a very high publicity. It is indexed and abstracted very quickly by Chemical Abstracts, EBSCO Publishing, ProQuest Science Journals, CAS Source Index (CASSI), Ulrich's Periodicals Directory, Google Scholar, etc. Since 2011 to 2014 *Sensors & Transducers* journal was covered and indexed by EI Compendex (CPX) index (including a Scopus, Embase, Engineering Village and Reaxys) in Elsevier products. The journal is included in the IFSA List of Recommended Journals (up-dated 9.12.2019), which contains only the best, established sensors related journals.

Topics of Interest

Include, but are not restricted to:

- Physical, chemical sensors and biosensors
- Digital, frequency, period, duty-cycle, time interval, PWM, pulse number output sensors and transducers
- Theory, principles, effects, design, standardization and modelling
- Smart sensors and systems
- Intelligent sensors and systems
- Sensor instrumentation
- Virtual instruments
- Sensors interfaces, buses and networks
- Signal processing, sensor fusion
- Remote sensing
- Frequency (period, duty-cycle)-to-code converters, ADC
- Technologies and materials
- Nanosensors and NEMS
- Microsystems
- Applications

Further information on this journal is available from the Publisher's web site:
http://www.sensorsportal.com/HTML/DIGEST/New_Digest.htm

Free Access and Subscriptions

Sensors & Transducers is the open access journal. All single articles are available for free download (article by article) without any registration and embargo period. For those who want to get the full page journal issue in print and/or pdf format there is an annual subscription. It includes 12 regular issues and some special issues. Annual subscription rates for 2020 are the following: Electronic version (in printable pdf format): 590.00 EUR; Printed with b/w illustrations: 950.00 EUR; 15 % discount is available for IFSA Members.

Further information about subscription is available on the IFSA Publishing's web site: http://www.sensorsportal.com/HTML/DIGEST/Journal_Subscription.htm

Advertising Information

Instructions for Authors

http://www.sensorsportal.com/HTML/DIGEST/Guides_for_Authors.htm

Call for Chapters

IFSA Publishing

Your Chapter may be in the next Volume of the popular Book Series

ADVANCES IN SENSORS: REVIEWS 8

Open Access Book Series

Sinse 2012

- Physical, chemical and biosensors
- Sensor uncertainty, accuracy, calibration
- Smart sensors and systems
- Intelligent sensors and systems
- Artificial Intelligence enabled sensors
- Virtual and soft sensors
- Sensor instrumentation
- Sensor buses and networks
- Signal processing, sensor fusion
- Nanosensors
- Photonic sensors
- Sensor interfacing and signal conditioning
- Materials for sensors
- MEMS, BioMEMS and NEMS
- Remote Sensors and Telemetry
- Sensor packages and reliability

https://www.sensorsportal.com/HTML/IFSA_Publishing.htm

IFSA

International Frequency Sensor Association Publishing

www.sensorsportal.com

ISSN 1726- 5479

9 771726 547001